On the influence of nucleation and growth of S_8 and Li_2S in lithium-sulfur batteries

Timo Danner[a,b,*], Arnulf Latz[a,b,c]

[a] *Institute of Engineering Thermodynamics, German Aerospace Center (DLR), Pfaffenwaldring 38-40, 70569 Stuttgart, Germany*
[b] *Helmholtz Institute Ulm for Electrochemical Energy Storage (HIU), Helmholtzstraße 11, 89081 Ulm, Germany*
[c] *Institute of Electrochemistry, University of Ulm, Albert-Einstein-Allee 47, 89081 Ulm, Germany*

Abstract

Lithium-sulfur (Li-S) batteries have the potential to outperform state-of-the-art lithium-ion batteries. One of the bottle necks is the limited power density which most conversion based systems have in common. One of the reasons is the formation of solid, insulating charge and discharge products which passivate active surfaces during operation of the cell. In depth knowledge of the formation and dissolution is needed in order to develop counter-measures overcoming the current limitations. In this article we present a continuum model of Li-S batteries including a detailed description of the formation and dissolution of solid particles based on the classical theory of nucleation and growth. By evolving a particle size distribution of the Li_2S and S_8 phase we are able to provide a qualitative description of the resulting particle morphology as well as their effect on active surface areas and transport pro-

---

[*] Corresponding author:
Email address: `Timo.Danner@DLR.de` (Timo Danner)
URL: `http://www.dlr.de/tt/en/` (Timo Danner)

cesses. Results of the simulations are in agreement with experimental data published in the literature. We perform intensive parameter studies which provide guidelines for the development of surface modifications enabling a spatial control of solid discharge product precipitation resulting in improved battery performance.

Keywords: lithium-sulfur batteries; continuum modeling; nucleation and growth; carbon doping; spatial control;

---

1. Introduction

Li-S batteries are promising candidates for the next generation of electrochemical energy storage devices [1]. Tremendous progress in practical electrode capacity and cycle life has been reported in the literature [2–5] which is the result of a careful optimization of electrode materials [6–11] and the electrolyte system [12–14]. Despite years of intensive research on novel materials and architectures several challenges are still obstructing the commercialization of the technology [15]. Certainly the well-known poly-sulfide shuttle is the major issue and an important research area in recent years was the development of polar and doped materials [10, 11] which are able to trap the dissolved species in the cathode. Another issue is the formation of solid charge and discharge products which are insulators and block active surfaces in the electrode. At low sulfur loading the use of high surface area carbons is a viable strategy to mitigate this issue [7]. However, in order to increase the energy density of the cells to a level which is competitive to state-of-the-art lithium-ion batteries a high sulfur loading and low electrolyte to sulfur ratio is inevitable. In practice this step often reduces the specific capacity of the cell, meaning the utilization of the available sulfur [16]. One strategy to overcome this limitation is a spatial control of the nucleation process as demonstrated by Yao *et al.* [17]. In practice the use of polar materials or doping might be feasible. However, in order to transfer this concept to real battery cells an improved understanding of the mechanisms governing the formation and dissolution of the solid charge and discharge products in Li-S batteries is indispensable. Recently, several groups studied the formation of Li_2S on model electrodes combining electrochemical techniques with ex-*situ* SEM imaging in order to correlate electrochemical performance with particle morphology [18–21]. The particle size and growth pattern was found to strongly depend on the material system and cell geometry as well as on the discharge current. However, in order to get a more comprehensive picture of the processes in the cell in-*situ* or in-*operando* techniques are required. The solid phases have a crystalline structure which makes X-ray based techniques the method of choice to study their formation and dissolution. In the literature there are several reports using in-*operando* techniques [22–28] during discharge to follow the dissolution and formation of S_8 and Li_2S, respectively. While these studies provide integral information on the growth process at different stages during discharge and charge they lack spatial resolution of the solid phases which is able to provide additional insights [29]. Recently, Yu *et al.* performed a comprehensive study using several synchrotron based techniques including XRD, X-ray tomography, and X-ray microscopy[30]. These studies provide a variety of additional information on the evolution and morphology of solid phases and serve as an excellent basis for parameterization and validation of modeling tools on the continuum scale. Several models for Li-S batteries were published in the literature investigating different aspects which infleunce the performance of Li-S batteries. The first continuum model of Li-S cells was developed by Kumaresan *et al.* [31] in order to simulate the discharge at different C-rates. The model was thoroughly investigated [32–35] and extended [36, 37] by other groups in order to simulate the charge processes, as well as electrochemical impedance spectra [38]. The important degradation mechanism of the polysulfide shuttle was addressed in [39, 40] and strategies to prevent the diffusion of polysulfides to the anode by structuring of the electrodes was investigated in [41, 42]. A study providing a mechanistic model of the nucleation and growth of Li_2S and S_8 particles during discharge and charge was published recently by Ren *et al.* [21, 43]. However, in their model they describe dissolution and precipitation of solids as a direct electrochemical step which results in qualitatively different growth mechanisms as discussed in Ref. [44]. Consequently, the results are not in agreement with experimental studies published in the literature [45, 20]. Andrei *et al.* derived a detailed model of the nucleation process using Kolmogorov-Avrami theory [44]. The model is able to provide qualitative description of the cell capacity for various discharge currents. The morphology or particle size distribution of the precipitate is not resolved in this study. In Ref. [46] a mesoscopic approach based on the kinetic Monte-Carlo technique was used to study various growth patterns which are observed experimentally and the effect on transport and kinetics was investigated by the same group in [47]. In this work we present a detailed model of the dissolution and formation of S_8 and Li_2S during charge and discharge which keeps track of the corresponding particle size distributions. The nucleation and growth process on a substrate consisting of multiple materials with different affinity to sulfur is described as a two-step mechanism using the classical theory of nucleation and growth [48] which was already successfully applied in the simulation of aqueous lithium-air batteries [49]. The parameters are derived based on DFT studies [50] and adjusted to represent experimental data. The model is able to provide a good qualitative description of different features observed in in-*operando* measurements published in the literature [30]. Based on these results different parameter studies are performed in order to investigate the sensitivity towards model parameters and their effect on capacity and discharge performance. Finally, we demonstrate the application of the model as an engineering tool to improve the capacity of the cell by taking into account the effect of hetero-atom doping. This highlights possible contributions of continuum models to improve the understanding as well as the performance of advanced Li-S batteries.

In the following chapter we provide a detailed derivation of our model including a discussion of model parameters. The results of the simulations are compared to in-*operando* data published in the literature in chapter 3.1 and 3.2 which serve as a basis for intensive parameter studies in the corresponding paragraphs. Finally, in section 3.3 we demonstrate the potential of our model in the optimization of cell capacity.

2. Theory

The model presented in this article is based on our previous theoretical work on Li-S batteries [40, 38]. The fundamental conservation equations for mass and charge in the electrolyte and solid phases are derived and solved in order to predict the behavior of Li-S batteries on the cell level. This approach allows monitoring of the local concentration and potential distributions in the electrode and electrolyte phase, as well as particle size distributions of solid charge and discharge products. This information enables the prediction of directions for material and cell design. In the next paragraphs we provide a detailed description and derivation of the simulation domain, governing equations, and simulation parameters.

Simulation domain. The one dimensional simulation domain as shown in Figure 1 consists of a porous sulfur-carbon composite cathode, a porous separator, and a Li metal anode. The porous cathode is made of a substrate (e.g. carbon) and sulfur particles which are simply mixed during slurry and electrode preparation. A melt infiltration process of sulfur in the nanopores of the substrate is not considered in this study [41]. Initially, the sulfur particles are assumed to be homogeneously distributed throughout the cathode with a uniform size distribution. During operation deposition of Li_2S and sulfur in the whole simulation domain is possible. In the study at hand we limit nucleation and growth events of solid phases to the cathode domain.

Transport equations. The electrolyte model describing the reaction and transport of dissolved species in the liquid electrolyte follows our earlier work on Li-S batteries [38, 40, 41]. Since the mechanism of polysulfide reduction is different in the various electrolyte solutions we use a reduced number of representative species in our simulations. An extension of the model to include additional representative polysulfide species is straight forward. The dissolved species i in this work are the polysulfides S_8, S_6^{2-}, S_4^{2-}, and S^{2-}, as well as the dissociated Li salt consisting of Li^+ cations, a generic monovalent

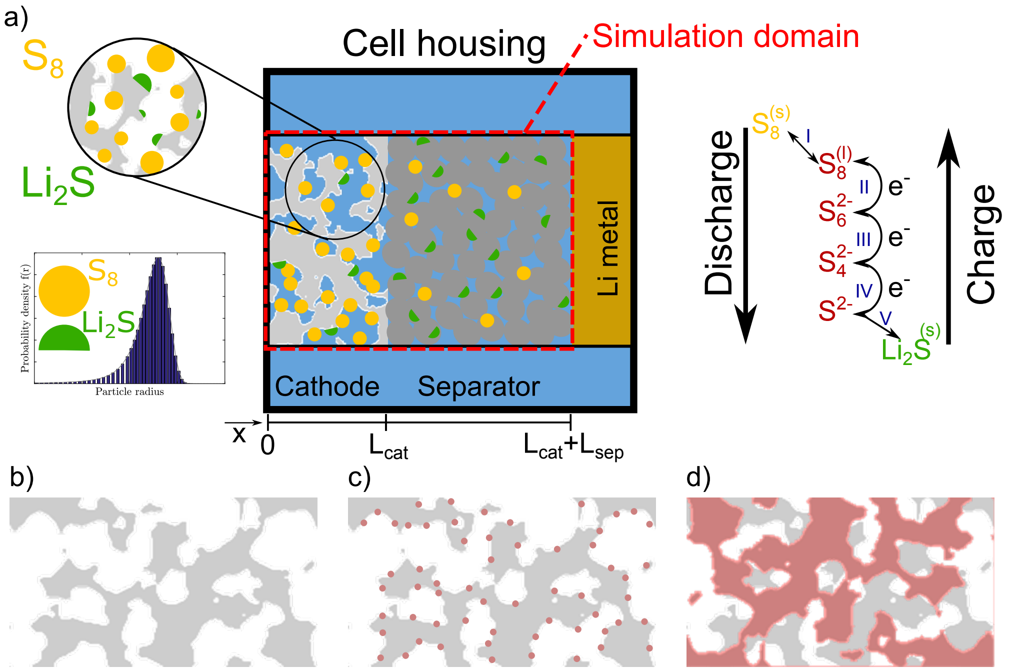

Figure 1: a) Schematic representation of the cell geometry consisting of a sulfur/carbon composite cathode, a porous separator, and a lithium metal anode. The red dashed box indicates the simulation domain. The sulfur oxidation/reduction mechanism is illustrated on the right hand side where dissolved polysulfide species are shown in red color and the solid products Li_2S and S_8 are displayed in green and yellow color, respectively. Figure b) - d) represent different scenarios of composite electrodes with b) pure carbon, c) doped carbon, and d) a mixture of carbon and a second material as host structure.

anion A^-, and NO_3^-. The addition of $LiNO_3^-$ reduces the polysulfide shuttle and in this contribution we assume a negligible effect of the polysulfide shuttle in the initial cycles. The conservation of mass of species i in the liquid electrolyte of the porous cathode and separator is given by

$$\frac{\partial \varepsilon_{\mathrm{elyte}} c_i}{\partial t} = -\frac{\partial N_i}{\partial x} + \sum_s \sum_m \nu_{i,m} \dot{s}_{s,m} \ , \qquad (1)$$

where N_i is the molar flux of species i and $\sum_s \sum_m \nu_{i,m} \dot{s}_{s,m}$ is a source term resulting from m chemical and electrochemical reactions on surface s (cf. Eq. (21)). Note, that this formulation using the electrode pore volume fraction $\varepsilon_{\text{elyte}}$ neglects additional electrolyte volume introduced during cell assembly. Recent studies show the enormous effect of electrolyte content on cell performance [51]. In order to understand the influence of the electrolyte reservoir in more detail 2D simulations would be needed which also resolve the transport in radial direction. The flux N_i of species i is described by the Nernst-Planck equation

$$N_i = -D_i^{\text{eff}} \frac{\partial c_i}{\partial x} - D_i^{\text{eff}} c_i \frac{z_i F}{RT} \frac{\partial \phi_{\text{elyte}}}{\partial x} \ , \tag{2}$$

where c_i and z_i are the concentration and charge number of species i, respectively. D_i^{eff} is an effective diffusion coefficient which takes into account the tortuosity of the porous medium. In our formulation we use the common Bruggeman correlation to describe this effect. Additionally, we account for the decrease of the mobility of species i due to an increase in electrolyte viscosity η_{elyte} at high polysulfide concentrations. The resulting expression of the effective diffusion coefficient follows as

$$D_i^{\text{eff}} = D_i^0 \varepsilon_{\text{elyte}}^{\beta} \frac{\eta_{\text{elyte}}^0}{\eta_{\text{elyte}}} \ , \tag{3}$$

where D_i^0 is the bulk diffusion coefficient, β the so-called Bruggeman coefficient of the pore network in separator and cathode, and η_{elyte}^0 the electrolyte viscosity at the initial salt concentration. Convective transport due to e.g. the dissolution and formation of solid species was found to provide a minor contribution to the species flux and is, therefore, neglected in this study. The ionic current in the electrolyte is given by the sum of all species fluxes

$$i_{elyte} = \sum_i z_i F \dot{N}_i \ . \tag{4}$$

The potential in the electrolyte is calculated according to the conservation of charge under the assumption of electro-neutrality

$$0 = -\frac{\partial i_{elyte}}{\partial x} + i_F + i_{DL} \ , \tag{5}$$

where i_F is the total Faradaic current given by the sum of all charge transfer reactions reactions

$$i_F = \sum_s a_s^v F \sum_m r_{m,s} \ , \tag{6}$$

and

$$i_{DL} = \sum_s a_s^v c_{DL} \frac{\partial \Delta\phi}{\partial t} \tag{7}$$

is the current resulting from the charging of the electrochemical double layer. During galvanostatic operation the double layer current is typically negligible compared to the Faradaic current. Due to global charge conservation the current in the support phase follows from

$$0 = \frac{\partial i_{elyte}}{\partial x} + \frac{\partial i_{elode}}{\partial x} \ . \tag{8}$$

The resulting transport equation for electrons in the support phase is given by

$$\frac{\partial i_{elode}}{\partial x} = \frac{\partial}{\partial x} \kappa_{elode}^{eff} \frac{\partial \phi_{elode}}{\partial x} = -i_F - i_{DL} \ , \tag{9}$$

where κ_{elode}^{eff} is the effective electrode conductivity. Note, that if multiple solid materials are present in the support an average potential of the solid phase is calculated by averaging the conductivity of the materials. The separator is assumed to be an insulating material with vanishing electric conductivity.

Boundary conditions. In our model we impose no-flux boundary conditions of dissolved species at $x = 0$ (cathode current collector) which results in

$$\left.\frac{\partial c_i}{\partial x}\right|_{x=0} = 0 \quad \text{and} \quad \left.\frac{\partial \phi_{\text{elyte}}}{\partial x}\right|_{x=0} = 0. \tag{10}$$

Due to charge conservation the boundary condition for the flux of electrons at $x = 0$ is given by

$$-\kappa_{elode}^{eff} \left.\frac{\partial \phi_{elode}}{\partial x}\right|_{x=0} = I \ , \tag{11}$$

where I is the current during galvanostatic operation. In the case of PITT simulations we directly set the cell voltage U for the potentiostatic operation according to $\phi_{elodes}|_{x=0} = U$. At the interface between cathode and separator ($x = L_{\text{cat}}$) all current is transported by the dissolved species in the liquid electrolyte and the corresponding boundary condition in the composite electrode is given by

$$\left.\frac{\partial \phi_{elode}}{\partial x}\right|_{x=L_{\text{cat}}} = 0 \ . \tag{12}$$

In the electrolyte we enforce a continuous flux of species mass and charge at $x = L_{\text{cat}}$ following Eq. (2). At the anode we model the plating/stripping of lithium according to Eq. (20). The potential of the Li electrode is set as reference

$$\phi_{elode}|_{x=L_{\text{cat}}+L_{\text{sep}}} = 0\text{V} \tag{13}$$

and the corresponding flux of Li^+ ions is modeled by a reaction expression according to Eq. (21). The flux of all other species is set to zero at the Li metal interface

$$N_i|_{x=L_{\text{cat}}+L_{\text{sep}}} = 0. \tag{14}$$

Electrochemical kinetics. The kinetic mechanism of sulfur reduction during discharge and oxidation upon charge is not yet totally understood. Several research groups try to shed some light on this issue combining electrochemical, [52–57], spectroscopic [58], and theoretical techniques [59, 60]. The reaction intermediates vary in the different studies depending on the solvent system. Kumaresan *et al.* [31] proposed a 5-step reduction from $\mathrm{S}_8^{(l)}$ down to S^{2-} where all intermediates except for S_6^{2-} are able to precipitate. Certainly the proposed mechanism is a simplification of reality and during charge and discharge additional reactions occur. Thus, a large number of parameters need to be determined by a fit to experimental data. This makes an unambiguous determination of parameters very challenging. In this context sophisticated models can also be used to evaluate experimental data for the quantification of process parameters.

In this study we use a reduced kinetic mechanism taking into account only representative species. Still, the characteristic shape of the discharge curve of a Li-S battery can be reproduced. The reduced reaction pathway is presented on the right hand side of Figure 1 a). First, $\mathrm{S}_8^{(s)}$ dissolves in the liquid electrolyte

$$\mathrm{S}_8^{(s)} \rightleftharpoons \mathrm{S}_8^{(l)} \; . \tag{15}$$

$\mathrm{S}_8^{(l)}$ is then reduced via

$$1/4\,\mathrm{S}_8^{(l)} + e^- \;\rightleftharpoons\; 1/2\,\mathrm{S}_6^{2-} \tag{16}$$

$$1/4\,\mathrm{S}_6^{2-} + e^- \;\rightleftharpoons\; 1/2\,\mathrm{S}_4^{2-} \tag{17}$$

$$1/6\,\mathrm{S}_4^{2-} + e^- \;\rightleftharpoons\; 4/6\,\mathrm{S}^{2-} \; . \tag{18}$$

Finally, the solid discharge product Li_2S precipitates according to

$$S^{2-} + Li^{+} \rightleftharpoons Li_2S^{(s)} \ . \tag{19}$$

At the Li metal anode the plating and stripping of Li is described by

$$Li^{+} + e^{-} \rightleftharpoons Li^{(s)} \ . \tag{20}$$

All reactions are assumed to be reversible.

In our model we employ an expression for the rate r_m of electrochemical reactions according to [61, 62]

$$r_{s,m} = k_{s,m}^{f,0} \frac{a_{\text{ed.}}^{1-\alpha} a_{\text{prod.}}^{\alpha}}{\gamma_{\ddagger}} \left(e^{-\frac{\alpha}{RT}\Delta\bar{\mu}_m} - e^{\frac{1-\alpha}{RT}\Delta\bar{\mu}_m} \right) \ , \tag{21}$$

where $k_{s,m}^{f,0}$ is the reaction rate constant, R is the ideal gas constant, and T is temperature. α and $\gamma_{\ddagger}$ are the symmetry factor and the activity coefficient of the transition state, respectively. The terms $a_{\text{ed.}}$ and $a_{\text{prod.}}$ represent the products of the activities according to

$$a_{\text{ed.}} = \prod_{\text{i=ed.}} a_i^{\nu_{i,m}} \quad \text{and} \quad a_{\text{prod.}} = \prod_{\text{i=prod.}} a_i^{\nu_{i,m}} \ , \tag{22}$$

where $\nu_{i,m}$ are the stoichiometric coefficients of the reaction. In this study all activity coefficients are assumed to be unity and activities follow as $a_i = c_i/c_{\text{ref}}$. The reference concentration c_{ref} is chosen to 1 mol/m^3 for all species. The electrochemical potential $\Delta\bar{\mu}_m$ of the chemical reaction m follows from the electrochemical potentials $\bar{\mu}_i$ of participating species i as $\Delta\bar{\mu}_m = \sum_i \nu_{i,m}\bar{\mu}_i$ which results in

$$\Delta\bar{\mu}_m = nF\eta = nF(\phi_{\text{elode}} - \phi_{\text{elyte}} - U_{\text{eq}}) \ , \tag{23}$$

where n is the number of electrons transferred in the charge-transfer reaction (CTR), F is Faraday's constant, ϕ_{elode} the potential of the electrode, ϕ_{elyte} the potential in the electrolyte and U_{eq} is the open circuit potential (OCP). It can be calculated according to

$$U_{\text{eq}} = U_{\text{eq}}^{\ominus} + \frac{RT}{F} \ln \frac{a_{\text{ed.}}}{a_{\text{prod.}}} \,, \tag{24}$$

where $U_{\text{eq}}^{\ominus}$ is the OCP at reference conditions. Note, that the resulting expression after inserting Eqs. (23) and (22) in (21) is similar to the well-known Butler-Volmer equation but can also be extended to different types of reactions [41, 61]. The resulting source terms $\dot{s}_{s,m}$ of the electrochemical reactions (16)-(18) are given by

$$\dot{s}_{s,m} = a_{s,m}^{v} \cdot r_{s,m} \,, \tag{25}$$

whereas the oxidation and reduction of lithium at the anode given by Eq. (20) is treated as a boundary condition at $x = L_{\text{cat}} + L_{\text{sep}}$.

Nucleation & growth. The passivation of electrochemical active surfaces and the clogging of pore space for ion transport due to the formation of solid charge and discharge products is crucial for the performance of the battery. In our simulations we take into account the dissolution and formation of S_8 and Li_2S during discharge and charge, respectively. The precipitation/dissolution reactions are given by Eqs. (15) and (19) of the proposed reaction mechanism. The driving force of the precipitation processes of the solid phase k is the so-called supersaturation $S_k = \frac{c_i}{c_i^s}$ of the liquid phase with precipitating species i. The solubility limit c_i^s is can be obtained from the solubility product K_k^{sp}. In the case of S_8 precipitation the supersaturation is defined by $S_{\mathrm{S}_8^{(s)}} = c_{\mathrm{S}_8}/c_{\mathrm{S}_8}^s$ where $c_{\mathrm{S}_8}^s$ is simply the solubility product $K_{\mathrm{S}_8^{(s)}}^{sp}$.

For Li_2S precipitation we use S^{2-} as key species to derive the precipitation mechanism since Li^+ ions are much more abundant in the electrolyte. We define the supersaturation $S_{\mathrm{Li_2S}} = c_{\mathrm{S^{2-}}}/c^s_{\mathrm{S^{2-}}}$ and obtain the solubility limit of S^{2-} via the solubility product $c^s_{\mathrm{S^{2-}}} = K^{sp}_{\mathrm{Li_2S}}/c^2_{\mathrm{Li^+}}$. In our simulations we keep track of the corresponding particle size distributions. S_8 precipitate is modeled to consist of spherical particles and Li_2S of hemispheres following the assumptions of Ren *et al.* [21]. In contrast to the precipitation model proposed by Ren *et al.* we treat the electrochemical reactions and the particle nucleation and growth as individual processes, separating the reduction/oxidation of polysulfides and particle growth. This allows us to use the framework of the classical theory of nucleation and growth (CNG) [48] which we applied successfully for the investigation of precipitation effects in aqueous Li-O_2 batteries [49]. In CNG the precipitation mechanism consists of two steps, namely the formation of a nucleus and subsequent particle growth. For the nucleation step it is assumed that the free energy of formation is given by a bulk term and a surface term

$$\Delta G_k = \Delta G^v_k + \Delta G^s_k \ . \tag{26}$$

The contribution of the bulk free energy is given by

$$\Delta G^v_k = -\frac{4}{3}\pi r^3_k \frac{RT \ln S_k}{v^m_k} \ , \tag{27}$$

where v^m_k is the molar volume of phase k. It is obvious that for concentrations above the solubility limit c^s_i ($S_i > 1$) precipitation of a solid phase is favorable. However, the formation of new crystal surfaces gives rise to an energy penalty in form of the surface contribution to the free energy

$$\Delta G^s_k = 4\pi r^2_k \gamma_k \ , \tag{28}$$

where γ_k is the surface energy of the newly formed crystal phase k. The resulting free energy for a given supersaturation has a maximum at a critical nucleus radius r_k^{crit} above which a stable growth process is possible. Below the critical radius the nucleus is likely to dissolve again. Inserting Eq. (27) and Eq. (28) in (26) and derivation with respect to r_k yields the critical radius according to

$$r_k^{\text{crit}} = \frac{2\gamma_k v_k^m}{RT\ln S_k} \ . \tag{29}$$

Inserting Eq. (29) one arrives at a critical energy of formation

$$\Delta G_k^{\text{crit}} = \frac{4}{3}\pi\gamma_k (r_k^{\text{crit}})^2 \ . \tag{30}$$

In the literature it is reported that the polysulfide species do have different affinities towards surfaces of different materials with nucleation sites l. In our simulations we take this into account by applying a correction ϕ_l term to the critical free energy [48]

$$\Delta G_{k,l}^{\text{crit,het}} = \phi_l \Delta G_k^{\text{crit}} = \frac{(2+\cos\theta_l)(1-\cos\theta_l)^2}{4}\Delta G_k^{\text{crit}} \ , \tag{31}$$

where θ_l is the contact angle of the newly formed nucleus with the nucleation site l. Thus, θ_l is the parameter controlling the affinity of the surface and nucleation sites towards polysulfide species and values of $\theta_l < 90\,\text{deg}$ indicate a high affinity towards polysulfide species. The nucleation rate is then described by an Arrhenius type equation with

$$\frac{\mathrm{d}\dot{n}'^{\text{nuc}}_{k,s,l}}{\mathrm{d}t} = a_s^v n_{k,s,l} k_k Z_{k,l}^{\text{het}} \exp\frac{-\Delta G_{k,l}^{\text{crit,het}}}{k_B T} \ , \tag{32}$$

where $n_{k,s,l}$ is the number of nucleation sites l of precipitating phase k per area of surface s, a_s^v is the specific surface area of surface s, k_k is the frequency factor of nucleation attempts, and $Z^{\text{het}}_{k,l}$ the Zeldovich coefficient taking into account the disintegration of newly formed nuclei. In our model we assume a diffusion controlled nucleation

$$k_k = D^{\text{red}}_i a_i^{-2} \; , \tag{33}$$

where $D^{\text{red}}_i = D^0_i \eta^{\text{elyte}}_0 / \eta^{\text{elyte}}$ is the diffusion coefficient reduced by viscosity effects in the electrolyte and $a_i = (c_i N_A)^{-\frac{1}{3}}$ is the typical length scale of the diffusion process given by the mean distance between two molecules of species i in solution. For the nucleation of Li_2S crystals we assume that the rate is limited by the availability of S^{2-} ions which have a much smaller concentration than Li^+ ions. Thus, we use the diffusion coefficient and concentration of S^{2-} for the calculation of the diffusion limited nucleation rate. The Zeldovich factor for heterogeneous nucleation on planar surfaces Z^{het} is given by [63]

$$Z^{\text{het}}_{k,l} = \frac{1}{\sqrt{\phi_l}} Z^{\text{hom}}_k = \frac{1}{\sqrt{\phi_l}} \sqrt{\frac{\Delta G^{\text{crit,het}}_{k,l}}{3\pi k_B T \tilde{N}^{\text{crit}}_k}} \; , \tag{34}$$

where $\tilde{N}^{\text{crit}}_k = 4/3\pi (r^{\text{crit}}_k)^3 N_A / v^m_k$ is the number of molecules in the critical nucleus of size r^{crit}_k.

In our simulations we investigate two different cases of surfaces as illustrated in Figure 1:

I) Homogeneous surfaces s where the nucleation site density $n_{k,s,l}$ on the uncovered surface area is determined by the size of the critical nucleus

$$n_{k,s,l} = 1/(\pi (r^{\text{crit}}_k)^2) \; . \tag{35}$$

II) Heterogeneous surfaces s with additional nucleation sites introduced by material modifications such as doping which have a different (typically higher) affinity for polysulfides. In this case $n_{k,s,l}$ changes over time due to nucleation of precipitate according to

$$\frac{\partial n_{k,s,l}}{\partial t} = -\frac{1}{a_s^v}\frac{\mathrm{d}\dot{n'}^{\mathrm{nuc}}_{k,s,l}}{\mathrm{d}t} , \tag{36}$$

The total nucleation rate of solid k on surface s is then given by the sum over all nucleation sites l

$$\frac{\mathrm{d}\dot{n}^{\mathrm{nuc}}_{k,s}}{\mathrm{d}t} = \sum_l \frac{\mathrm{d}\dot{n'}^{\mathrm{nuc}}_{k,s,l}}{\mathrm{d}t} . \tag{37}$$

The subsequent growth step is in the classical theory of nucleation and growth described as a two step process consisting of diffusion to and reaction on the particle surface. The growth rate in radial direction is given by [48]

$$\frac{\mathrm{d}r_k}{\mathrm{d}t} = \frac{v_k^m D_i^{\mathrm{red}}\left(c_i - c_i^s\right)}{r_k + \frac{D_i^{\mathrm{red}}}{k_k^0}} , \tag{38}$$

where k_k^0 is the rate constant of the chemical reaction on the surface of solid phase k. This reaction mechanism is valid only for first order kinetics of the reacting species. In the case of $\mathrm{Li_2S}$ growth we assume that the growth process is dominated by S^{2-} due to the already mentioned large excess of lithium ions. Other reaction mechanisms are possible in this framework, however, the calculation of growth rates will become more challenging. Note, that Eq. (38) intrinsically takes into account the dissolution of particles if the concentration c_i is below the solubility limit c_i^s. In order to monitor the evolution of particle sizes of phase k on active surfaces s during operation of the battery we keep track of size distributions $f_{k,s}(r_k)$ of spherical $\mathrm{S_8}$ or hemispherical $\mathrm{Li_2S}$ particles by means of population balances according to

$$\frac{\partial f_{k,s}(r_k)}{\partial t} = -\frac{\partial}{\partial r_k}\left(f_{k,s}(r_k)\frac{\mathrm{d}r_k}{\mathrm{d}t}\right) , \tag{39}$$

where the right hand side of Eq. (39) describes the so-called property convection which is in this case simply the growth of particles. As boundary conditions for this equation we model the nucleation of particles with $r_k = r_k^{\min}$ if $S_k > 1$ and the complete dissolution of particles of radius $r_k^{\min}$ if $S_k < 1$.

$$f_{k,s}(r_k)\frac{dr_k}{dt}\bigg|_{r=0} = \psi_{k,s}^{\min} \tag{40}$$

$$\psi_{k,s}^{\min} = \begin{cases} \frac{\mathrm{d}\dot{n}_{k,s}^{\mathrm{nuc}}}{\mathrm{d}t} & \text{for } S_k > 1 \\ f_{k,s}(r_k^{\min})\frac{v_k^m D_i^{\mathrm{red}}\left(c_i - c_i^s\right)}{r_k^{\min} + \frac{D_i^{\mathrm{red}}}{k_k^0}} & \text{for } S_k <= 1 \end{cases} \tag{41}$$

Additionally, we enforce that no particle can become larger than the maximum pore radius r_{pore}^{max}

$$\frac{dr_k}{dt}\bigg|_{r=r_{pore}^{max}} = 0. \tag{42}$$

The particle size distributions contain the relevant information on the macroscopic scale for the calculation of the volume fraction of spherical $\mathrm{S_8}$

$$\varepsilon_{\mathrm{S_8}} = \sum_s \int_{r_{\mathrm{S_8}}=0}^{r_{\mathrm{S_8}}=r_{pore}^{max}} \frac{4}{3}\pi r_{\mathrm{S_8}}^3 f_{\mathrm{S_8},s}(r_{\mathrm{S_8}}) dr_{\mathrm{S_8}} \tag{43}$$

and hemi-spherical $\mathrm{Li_2S}$ particles, respectively.

$$\varepsilon_{\mathrm{Li_2S}} = \sum_s \int_{r_{\mathrm{Li_2S}}=0}^{r_{\mathrm{Li_2S}}=r_{pore}^{max}} 0.5\frac{4}{3}\pi r_{\mathrm{Li_2S}}^3 f_{\mathrm{Li_2S},s}(r_{\mathrm{Li_2S}}) dr_{\mathrm{Li_2S}} \tag{44}$$

Active surface areas are given by

$$a_s^v = a_s^{v,0} - \sum_k \int_{r_k=0}^{r_k=r_{pore}^{max}} \pi r_k^2 f_{k,s}(r_k) dr_k\ , \tag{45}$$

where $a_s^{v,0}$ is the initial active surface area. Finally, the source terms $\dot{s}_{s,m}$ entering the conservation equations of the species i participating in the precipitation/dissolution reactions $m = 1, 5$ are given by

$$\dot{s}_{s,1} = \frac{1}{v^{m}_{\mathrm{S}_8}} \int_{r_{\mathrm{S}_8,\mathrm{s}}=0}^{r_{\mathrm{S}_8,\mathrm{s}}=r^{max}_{pore}} \frac{4}{3}\pi r^{3}_{\mathrm{S}_8,\mathrm{s}} \frac{\partial}{\partial r_{\mathrm{S}_8,\mathrm{s}}} \left(f_{\mathrm{S}_8,s} \frac{\mathrm{d}r_{\mathrm{S}_8,\mathrm{s}}}{\mathrm{d}t} \right) dr_{\mathrm{S}_8,\mathrm{s}} \tag{46}$$

$$\dot{s}_{s,5} = \frac{0.5}{v^{m}_{\mathrm{Li}_2\mathrm{S}}} \int_{r_{\mathrm{Li}_2\mathrm{S},\mathrm{s}}=0}^{r_{\mathrm{Li}_2\mathrm{S},\mathrm{s}}=r^{max}_{pore}} \frac{4}{3}\pi r^{3}_{\mathrm{Li}_2\mathrm{S},\mathrm{s}} \frac{\partial}{\partial r_{\mathrm{Li}_2\mathrm{S},s}} \left(f_{\mathrm{Li}_2\mathrm{S},s} \frac{\mathrm{d}r_{\mathrm{Li}_2\mathrm{S},\mathrm{s}}}{\mathrm{d}t} \right) dr_{\mathrm{Li}_2\mathrm{S},\mathrm{s}} \tag{47}$$

2.1. Parameters

Model parameters in this study were chosen to represent the geometry and electrochemical performance of the cell presented in [30]. If possible the physical parameters were compiled from different sources in the literature to improve the qualitative predictions of the model. Still, there is a number of unknown parameters which were determined by fitting the electrochemical measurements in [30].

Geometry parameters. The Li-S cell which was simulated in this work consists of a porous S/C composite cathode, a separator and a Li metal anode. A schematic image of the simulation domain is shown in Figure 1. The composite cathode consists of a carbon fiber layer which is coated with a sulfur/carbon slurry. The total thickness of the electrode is 100 µm and the estimated specific surface area is $1 \cdot 10^6$ m^{-1}. In our simulations we assume an integral initial composition of the electrode of 19 vol-% carbon and binder and 1.2 vol-% of sulfur. The initial volume fraction of $\mathrm{Li_2S}$ is negligible. The separator has a thickness of 100 µm and a nominal porosity of around 80 %.

Electrolyte parameters. The liquid electrolyte is parametrized for a mixture of DOL:DME with 1M LiTFSI and 0.2M $\mathrm{LiNO_3}$ which is a common electrolyte in the LiS community. In our model we employ dilute solution theory for transport in the electrolyte in order to work with a smaller number of unknown parameters. The effect of reduced transport properties due to an increase in electrolyte viscosity is taken into account by (3) and a correlation of the electrolyte viscosity on total sulfur concentration is given by [51]

$$\eta_{\text{elyte}} = 9.8471 \cdot 10^{-3} \cdot \exp\left(3.5338 \cdot 10^{-4} \cdot c_S\right) \ , \tag{48}$$

where c_S is the total sulfur concentration in mol/m^3 and we assume similar trends in DOL:DME and TEGDME. A summary of the diffusion coefficients including sources is given in Table 2.

Electrochemical reactions. In our model we use a reduced reaction mechanism to describe the reduction and oxidation of dissolved polysulfide species given by Eqs. (16)-(18). The parameters of the electrochemical reactions are the exchange current density, open circuit potential at reference conditions, and the symmetry factor of the transition state. The parameters are adjusted to reproduce the discharge curves in [30] and are summarized in Table 2.

Solid phase dissolution & growth. The parameters of the nucleation and growth models of S_8 and Li_2S are the solubility K_k^{sp}, the surface energy γ_k of the solid phases and the kinetic factor of the growth reaction k_k^0. Initial guesses for the surface energy of S_8 and Li_2S are taken from the literature [50] and were in a next step adjusted to give a better representation of the experimental data. Values for the solubility of sulfur can be readily obtained from the literature [64], however, data for Li_2S could not be found and we estimate a value of $1.55 \cdot 10^7$ which qualitatively reproduces discharge curves and particle size distributions. In a similar procedure the kinetic constants of the dissolution and growth reactions were determined. The kinetic constant of S_8 dissolution was adjusted to reproduce the capacity in the upper discharge plateau and the kinetic constant of Li_2S was chosen to match the capacity of a C/10 discharge [30]. At the beginning of the discharge process the number of Li_2S particles is negligible and the initial sulfur content and distribution of S_8 particles is estimated from the distribution images in Ref. [30]. All Parameters of the nucleation and growth models are listed in Tables 1 and 2.

Simulation parameters. All model equations are implemented and solved in Matlab with the initial conditions, cell geometry, and model parameters given in Tables 1 and 2, respectively. The simulation time of a galvanostatic discharge is in the order of minutes up to a few hours depending on the discretization and operation conditions. The simulation studies presented in this work use one representative volume element for the cathode domain. This provides comparable results to the integral XRD and X-ray microscopy measurements and reduces the computational load. Simulation results with higher spatial resolution are provided in the electronic supplementary information.

3. Results and discussion

In this section we present simulation results of our newly devised Li-S cell model which takes into account the dissolution, nucleation and, growth of solid S_8 and Li_2S during discharge and charge. As outlined in the previous paragraph a number of model parameters are estimated by fitting experimental data published in the literature [30]. Although, the qualitative agreement of our simulation results with the experimental data is favorable this type of parameter estimation is certainly prone to errors. Therefor, the aim of this study is to analyze and predict qualitative trends. In the future further model experiments are needed to fix some of these parameters which will increase the reliability of model predictions.

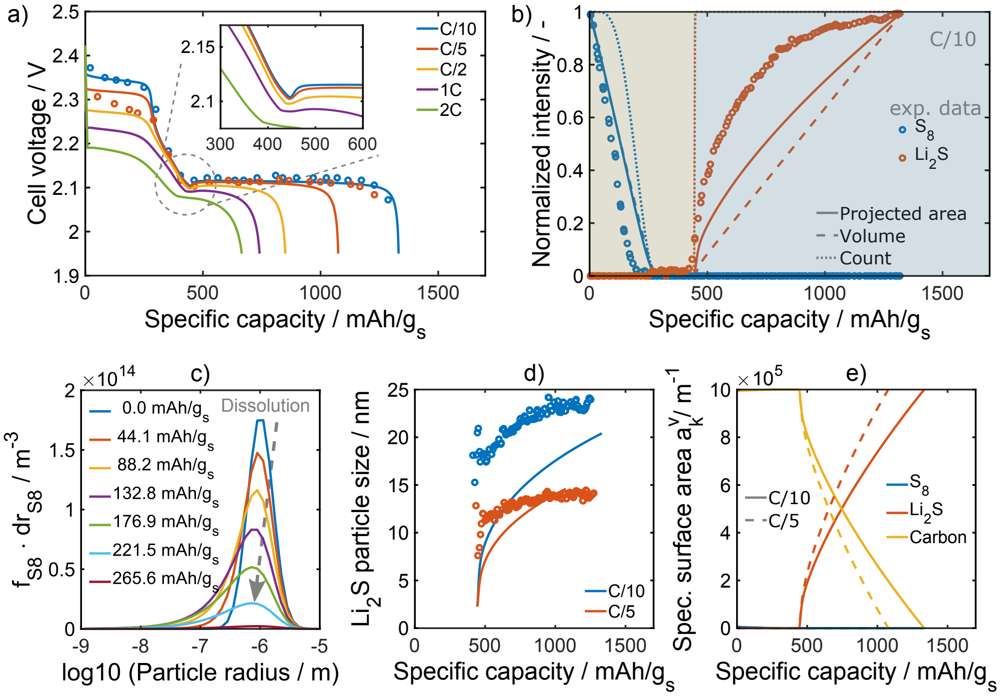

Figure 2: Representative results of galvanostatic discharge simulations. a) Discharge curves at various C-rates. The inset shows a magnification of the region with the voltage dip at low C-rates. b) Normalized intensities of solid S_8 (blue) and Li_2S (red) during a C/10 discharge. Lines represent simulation results which are calculated based on the total projected area (solid), total volume (dashed), and total particle number (dotted). c) Evolution of the S_8 particle size distribution during the dissolution in the first voltage plateau. d) Evolution of Li_2S particle size at C/10 (blue) and C/5 (red) during the second voltage plateau. e) Specific surface area of solid phases during C/10 and C/5 discharge. The experimental data provided by closed symbols in the graphs above is taken from Ref. [30].

3.1. Discharge

In this first section processes happening during the discharge of a Li-S cell are discussed. The results are split in three paragraphs. First, the results during a galvanostatic discharge are analyzed. Second, a sensitivity analysis of parameters of the nucleation and growth model is performed. Third, a potentiostatic intermittent titration experiment is simulated in order to elucidate the Li_2S growth mechanism.

Discharge curves. Figure 2 a) presents results of galvanostatic discharge simulations at various C-rates. The discharge curve at C/10 rate shows two voltage plateaus which is commonly observed during discharge of a Li-S battery. Between the two plateaus there is a steep decrease in cell voltage with a small dip below the average cell voltage of the second plateau. This dip is less pronounced at higher currents and can be linked to the nucleation of Li_2S crystals. With increasing C-rate the simulations predict a decrease in cell voltage as well as capacity which is commonly also observed in experimental studies. The simulations are able to reproduce the experimental data taken from Ref. [30] at C/10. However, the loss in capacity at higher currents is more pronounced. In order to link the features of the discharge curves with the formation and dissolution of solid phases Figure 2 b) shows the normalized intensity of S_8 and Li_2S. Closed symbols represent the data of *operando* X-ray diffraction measurements [30] and the lines are calculated based on simulation results. The solid line represents the integral projected surface area of all particles normalized by the maximum value, and the dashed and dotted lines are the normalized volume fractions and total particle number, respectively. The simulations show that during the first plateau all sulfur particles slowly dissolve in the electrolyte. After a transferred charge of around 250 mAh/g$_S$ basically all sulfur particles are dissolved. These simulation results are in line with the *operando* measurements. The intensities calculated based on the volume fraction and projected surface area are very similar. The dotted line representing the normalized total particle density decreases at a slightly higher transferred charge because during the dissolution process the particles first start to shrink before they totally dissolve. This process is shown in Figure 2 c). The dark blue line presents the initial sulfur distribution at the beginning of the discharge process. In the first voltage plateau the number of particles a well as the mean particle diameter decreases until all particles are basically dissolved at around 250 mAh/g$_S$. In the sloping voltage region between 250 and 500 mAh/g$_S$ basically all the sulfur is in solution. At 500 mAh/g$_S$ a strong increase in Li_2S intensity can be observed. This is in line with the experimental data and clearly links the small dip in cell voltage to the formation of Li_2S. The total particle density in our simulations jumps to one which shows that all Li_2S particles are formed in this initial nucleation period and afterwards only particle growth can be observed. Therefore, the increase in the volumetric intensity is linear in the second voltage plateau. The normalized total projected surface area shows a similar trend like the experimental data with a steep increase in the initial stage which reduces towards higher capacity. This indicator is closest to the experimental signal measured by XRD since the intensity of the signal is correlated with the area hit by the X-ray beam. However, in the experiments the signal is collected integrally through the cell and the full diameter of particles which are hidden by particles closer to the X-ray source are not fully taken into account. Since in the simulations the signal is calculated from the projected surface area of all particles deviations in intensity are expected. During this initial stage a fast growth of the average Li_2S particle size can be observed which is shown in Figure 2 d). This is typical for a so-called burst nucleation mechanism. In the simulations the particle growth rate is slightly faster compared to the experimental data indicating that the kinetic rate constant $k^0_{\mathrm{Li_2S}}$ might be smaller than the value which was chosen based on the fit of the discharge curve. At the end of the discharge process the Li_2S particles form a film on the carbon host material which passivates the reactive surface. The evolution of projected S_8 and Li_2S surface area as well as the carbon active surface area are shown in Figure 2 e). The large sulfur particles block a comparatively small fraction of the active carbon surface and can be barely seen in the graph. The large number of Li_2S particles in turn rapidly block the carbon surface and reduce the specific carbon surface area until at the end of the discharge process the whole surface is passivated by Li_2S precipitate causing the drop in cell voltage.

Sensitivity analysis. In order to study the sensitivity of our model towards a variation of the input parameters of the nucleation and growth models we perform a comprehensive sensitivity analysis. Figure 3 a) shows the relative sensitivity of the cell capacity $C(x)$ towards a parameter x.

$$\text{Sensitivity}_i = \frac{(C(x^0) \;-\; C(x^0 + \Delta x))/C(x^0)}{(x^0 \;-\; x^0 + \Delta x)/x^0} \; . \tag{49}$$

The graph highlights the significant influence of Li_2S formation on cell performance during discharge. Therefore, the focus of this paragraph is set on the analysis of the effect of Li_2S surface energy on cell performance. The pa-

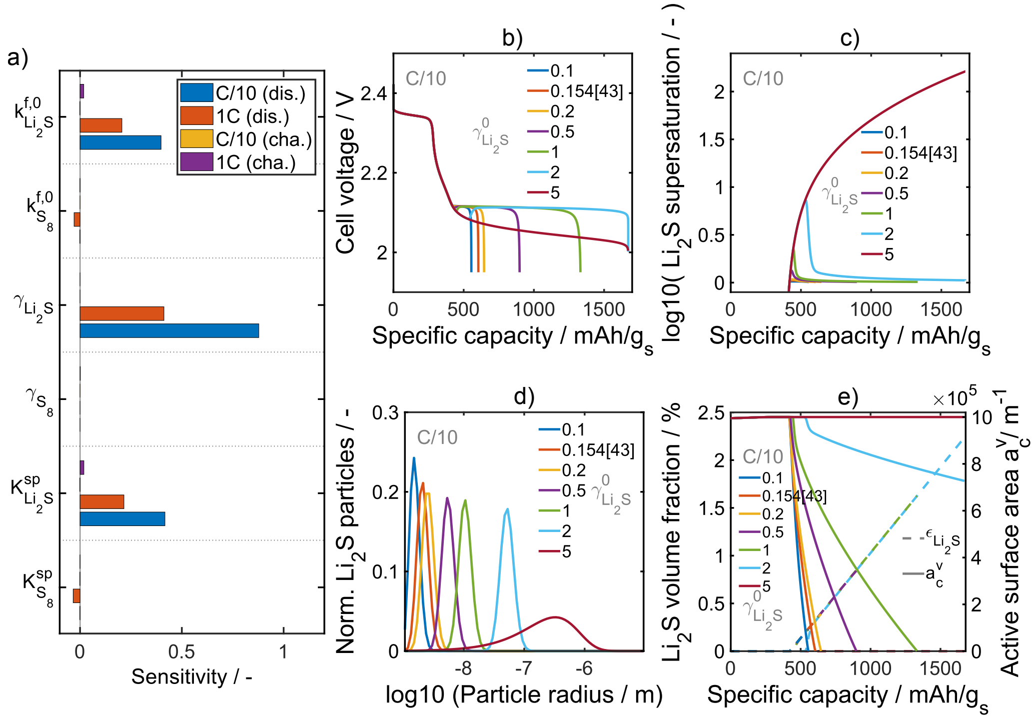

Figure 3: a) Relative sensitivity of the cell capacity for selected model parameters of the S_8 and Li_2S nucleation and growth models. Discharge curves (b)), supersaturation (c)), particle number (d)), and volume fraction (e)) for different values of the Li_2S surface tension γ_{Li_2S} varied around the initial surface tension $\gamma^0_{Li_2S}$.

rameters of S_8 dissolution and growth have a minor impact on cell capacity during discharge and charge of the battery. A parameter study of S_8 surface energy during charge is discussed in the next section. Figure 3 b) presents discharge curves of a Li-S cell with a Li_2S surface energy varying between 0.1 and 5 times the standard surface energy $7.7 \cdot 10^{-3}$ J/m^2 given in Table 2. Results of a simulation with a surface energy calculated in DFT simulations are presented in the curve with $0.154{\cdot}\gamma^0_{Li_2S}$. The simulations show that with increasing surface energy the voltage dip at the beginning of the second plateau becomes more pronounced and shifts towards higher depth of discharge. At $\gamma_{\mathrm{Li_2S}} = 5\gamma^0_{\mathrm{Li_2S}}$ the dip vanishes altogether which indicates that the nucleation of $\mathrm{Li_2S}$ seed crystals is largely suppressed. As a result the supersaturation of the electrolyte shown in Figure 3 c) increases with $\mathrm{Li_2S}$ surface energy. Following Eq. (26) a higher supersaturation is needed to overcome the nucleation barrier of seed crystals. At the maximum of the supersaturation the nucleation and growth of $\mathrm{Li_2S}$ particles is triggered and $\mathrm{S^{2-}}$ and $\mathrm{Li^+}$ are consumed rapidly which again reduces the supersaturation. The continuous increase of $\mathrm{Li_2S}$ supersaturation for $\gamma_{\mathrm{Li_2S}} = 5\gamma^0_{\mathrm{Li_2S}}$ confirms the negligible nucleation rate of $\mathrm{Li_2S}$ crystals. In conclusion the total number of particles is reduced at higher surface energies and at the same time a larger concentration of $\mathrm{S^{2-}}$ ions in the electrolyte favors the growth of large particles. The resulting $\mathrm{Li_2S}$ particle size distributions at the end of the discharge process are shown in Figure 3 d). As expected the graph confirms a significant increase in $\mathrm{Li_2S}$ particle size. This has important implications because small particles readily block the active surface area and limit the capacity of the cell. Figure 3 e) shows the evolution of $\mathrm{Li_2S}$ volume fraction and active surface area. The temporal evolution of the $\mathrm{Li_2S}$ volume fraction of different surface energies differs only in the initial stage after the nucleation process. Afterwards we observe a linear increase in volume fraction except for the last case with $\gamma_{\mathrm{Li_2S}} = 5\gamma^0_{\mathrm{Li_2S}}$ where no significant amount of $\mathrm{Li_2S}$ is formed. Consequently, there is no passivation of the carbon surface until the end of the discharge process. With decreasing surface energy the reduction in active surface area becomes more pronounced and at $\gamma_{\mathrm{Li_2S}} = 0.1\gamma^0_{\mathrm{Li_2S}}$ the whole surface is blocked only a few minutes after the initial nucleation event.

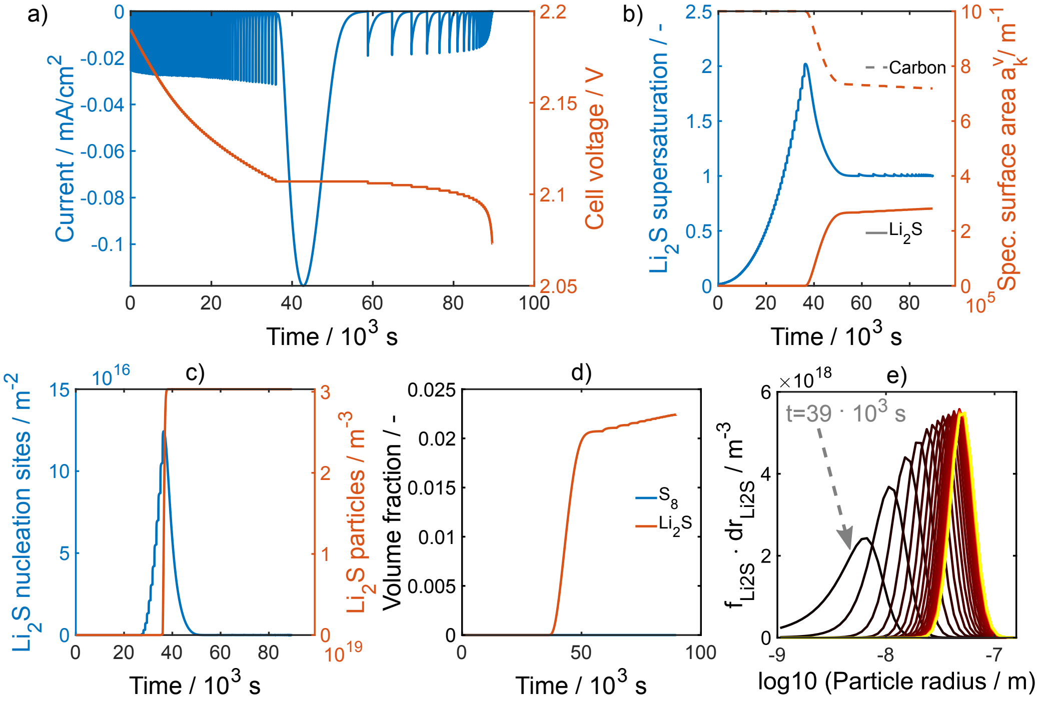

Figure 4: Simulation results of a potentiostatic intermittent titration technique (PITT) study between 2.19 and 2.07 V with voltage steps of 1 mV. a) Current and voltage signals. b) Supersaturation and specific surface area. c) Available nucleation sites and total number of Li_2S particles. d) S_8 and Li_2S volume fraction. e) Evolution of the Li_2S particle size distribution after the initial nucleation event.

This study indicates that an engineering of the nucleation barrier by modifications of the electrode surface will be able to provide an increase in cell performance.

Potentiostatic Intermittent Titration Technique. In the literature the Potentiostatic Intermittent Titration Technique (PITT) was suggested to study the influence of different materials and cell compositions, e.g. the sulfur-to-electrolyte ratio, on the nucleation and growth of Li_2S crystals during discharge [18, 20]. It was found that the current signal of the PITT measurements gives important insights on the growth mechanism. Therefore, we present results of a simulated PITT experiment in Figure 4. First, we simulate a discharge of the cell down to 2.19 V in order to fully dissolve all solid sulfur in the electrolyte. Then the cell voltage is reduced in steps of 1 mV down to a lower cut-off voltage of 2.07 V. In each step the cell voltage is kept constant until the current drops below $-1\cdot10^{-3}$ mA/cm^2. Figure 4 a) presents the corresponding current and voltage signals over time for the procedure outlined above. During the initial steps the current signal decays in a few seconds below the current threshhold and the cell voltage decreases rapidly. Slightly above 2.1 V we observe a peak in the current signal followed by a relatively long CV phase where a significant amount of charge is transferred. The cell voltage corresponding to the current peak coincides with the minimum of the voltage dip during galvanostatic discharge at small currents. Subsequent voltage steps are again much shorter and the current drops rapidly below the threshhold. At the end of the simulation the potential steps are very short indicating a full reduction of all sulfur species. The qualitative trends of this simulated PITT experiment are in line with experimental data reported in the literature [20]. This result provides additional evidence that the solution based precipitation and dissolution mechanism described in this work is able to represent the processes in Li-S batteries and should be probably considered as well in other studies which treat the growth of Li_2S particles in one step following the theories developed for electro-deposition. During the first phase the reduction of cell voltage leads to an increase in S^{2-} concentration in the electrolyte and, thus, increases the supersaturation of

Li_2S (cf. Figure 4 b)). After $39 \cdot 10^3$s the supersaturation reaches a maximum. At this point the volume term in Eq. (26) is equal to the surface energy and at only slightly larger concentrations of S^{2-} nucleation of seed crystals with subsequent particle growth can be observed. Figure 4 c) shows the number of nucleation sites per active surface area. In our model we assume that the number of nucleation sites is inversely proportional to the critical radius (Eq. (35)). Therefore, the number of nucleation sites increases with supersaturation because at higher supersaturation the critical radius decreases. At the maximum of the supersaturation a so-called burst nucleation event occurs and all the Li_2S particles are formed in a very short nucleation phase. As a result we observe a sudden increase in Li_2S volume fraction as shown in Figure 4 d) as well as reduction in active surface area shown in Figure 4 c). However, even at the end of the PITT experiment the active surface is not fully covered with precipitate as indicated by the red lines in Figure 4 b). The evolution of the Li_2S particle size distribution is shown in Figure 4 e). Starting shortly after the initial nucleation stage the graph illustrates the growth process of Li_2S particles. During the subsequent CV steps the particles slowly start to grow which is indicated by the change in color from black to yellow. At the end of the PITT simulation the growth process is relatively slow since most of the polysulfides are consumed in the first long voltage step following the nucleation events.

3.2. Charge

After a detailed discussion of the Li_2S nucleation and growth process governing the discharge of the battery in the previous section the focus of this section will be on battery charge. Like in the last section we will first analyze

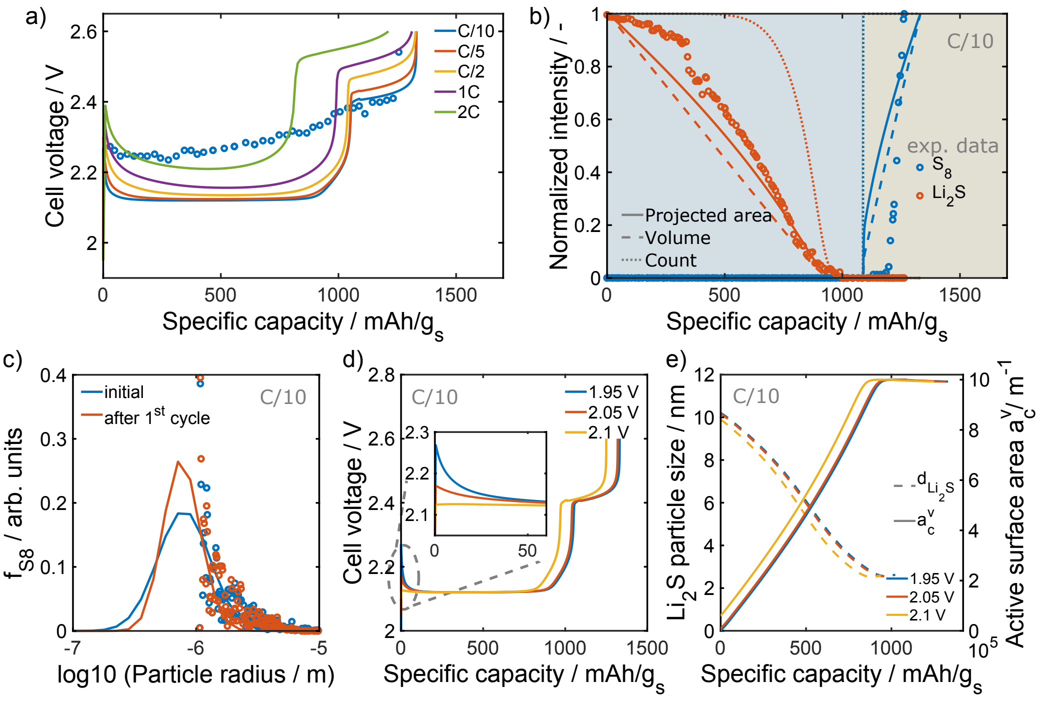

Figure 5: Results of charge simulations of a Li-S battery. a) Charge curves at various C-rates after a C/10 discharge. b) Normalized intensities of solid S_8 (blue) and Li_2S (red) during a C/10 charge. Lines represent simulation results which are calculated based on the total projected area (solid), total volume (dashed), and total particle number (dotted). c) S_8 particle size distribution in the initial state before the first discharge (blue) and after the first charge at C/10 (red). d) Charge curves of a C/10 charge after discharge to different cut-off voltages. e) Evolution of Li_2S particle size and active surface area during a C/10 charge process after discharge to a lower cut-off voltage of 1.95V, 2.05V, and 2.1V. The experimental data provided by the symbols in the graphs above is taken from Ref. [30].

the processes governing the charge process, followed by a parameter study of the effect of Li_2S solubility and S_8 surface energy. Finally, we investigate the influence of charge rate on S_8 particle size in the last paragraph of this section.

Charge curves. Figure 5 a) shows the cell voltage of the Li-S cell during the charge process at various C-rates after a subsequent C/10 discharge. In the first stage of the charge process there is a small peak in cell voltage at low currents which can be also found in the experimental data. In the simulations this is due to the initial dissolution of Li_2S particles blocking the active surface of the cathode. At C/10 the first voltage plateau is in the simulations around 100 mV lower in cell voltage. We have to stress that we use in our simulations the same parameters and reaction mechanism in all simulations. Therefore, the discrepancy between simulation and experiment during this first stage of the charge process might be due to a different mechanism for sulfur oxidation or an insufficient parameterization of some of the model parameters which could not be identified during the analysis of the discharge process. This issue will be discussed in more detail in the following paragraph. In the second stage of the charge process the cell voltage of the simulations is in good agreement with the experimental data at low C-rates. In the simulations we also see a very small dip in the cell voltage at the beginning of the plateau which marks the onset of S_8 nucleation and growth. The evolution of solid phases during the charge process at C/10 rate is shown in Figure 5 b). During the first stage Li_2S particles dissolve in the liquid electrolyte. The simulations provide a good qualitative description of the experimental data. This indicates that the time scale of the dissolution process is well reproduced. At around 1100 mAh/g_s we can observe the initial phase of S_8 formation which coincides with the voltage feature described above. In the experimental data the formation of S_8 is observed at slightly higher DOD. Such an effect might be due to an underestimation of S_8 surface energy or growth rate. Still, the final particle size distribution of S_8 after the charge process shown in Figure 5 c) is in qualitative agreement with the data extracted from the images given in Ref. [30]. In their *operando* X-ray tomography data the authors observe a more homogeneous distribution of smaller particles compared to the initial distribution in the pristine state which is in line with the predictions of our simulations. The final particle size strongly depends on the current during the charge process which is discussed in paragraph 3.2.

Parameter studies. In order to analyze and provide estimates for the aforementioned uncertainties in the assumed sulfur oxidation mechanism and model parameterization we perform parameter studies to supplement the sensitivity analysis given in Section 3.1. Figure 6 a) shows simulated charge curves for varying Li_2S solubility. The simulations show that an increasing solubility decreases the cell voltage in the first plateau. This shows that Li_2S solubility indeed affects the position of this first plateau and indicates that the solubility might be even lower than the values assumed in our simulations. However, it was not possible to simulate smaller solubilities because the amount of S^{2-} dissolved in the electrolyte was too small to provide a sufficient supply of polysulfides to sustain the small currents of a C/10 rate. The second voltage plateau corresponding to S_8 precipitation and growth is not affected by Li_2S solubility. Figures 6 c) and d) show the corresponding normalized intensities and specific surface areas of S_8 and Li_2S. Increasing solubility shifts the Li_2S intensity to lower capacities, thus also affecting the time scale on which Li_2S is dissolved. The same trend is also reflected in the

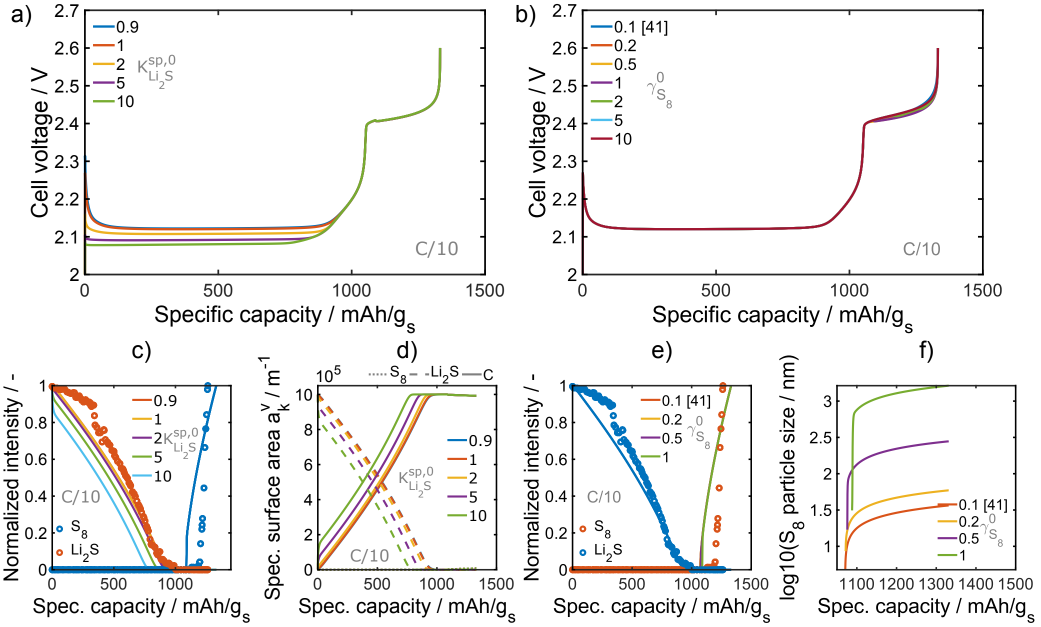

Figure 6: Simulated charge curves for different values of a) Li_2S solubility and b) S_8 surface energy. The parameters are varied around the model standard value (superscript 0, cf. Table 2) to investigate the effect of Li_2S solubility on the c) normalized Li_2S intensity and d) specific surface area, as well as the influence of S_8 surface energy on e) normalized S_8 intensity and f) particle size. The experimental data provided by open symbols in the graphs above is taken from Ref. [30].

evolution of Li_2S specific surface area. This is another indication that the solubility in the ether-based electrolyte is even lower than assumed in the simulations. In the discharge simulations we observed a tremendous effect of the Li_2S surface energy on particle size and capacity. During charge a similar effect of the S_8 surface energy is expected. However, even a variation of the surface energy by two orders of magnitude does not significantly affect the resulting charge capacity. This is in line with the small sensitivity determined in the sensitivity analysis. As shown in Figure 5 b) the onset of

S_8 formation occurs at slightly smaller capacity in the simulations compared to the experimental data. As indicated by our simulations shown in Figure 6 e) higher surface energy shifts this onset to higher capacity, however, at the same time it has a significant effect on the resulting S_8 particle size. A small surface energy, corresponding to DFT data published in the literature [50], results in S_8 particles of only a few nanometers as shown in Figure 6 f), which is in contradiction to the relatively large sulfur cluster observed in the in-*operando* tomography data[30]. However, a significantly larger surface energy than the standard value chosen in our simulations will cause the growth of large particles even exceeding the pore diameters of the carbon host material, limiting the reasonable parameter range to the window shown in Figure 6 e) and f). As discussed in the previous paragraphs, other choices of parameters might provide an improved agreement with the experimental data. Additional dedicated measurements of the parameters discussed above are needed to improve the accuracy of the simulations. Beyond that, sophisticated models can help to extract parameters from the additional information provided by in-*operando* studies in an inverse modeling approach.

Effect of current. An important factor for the development of future Li-S batteries is the rate capability of the batteries enabling e.g. fast charging applications in the mobility sector. Thus, it is important to understand the effect C-rate on the morphology of resulting S_8 precipitate in the fully charged state. Figure 7 a) shows the voltage profile of a simulated shallow cycling experiment. In a first step the cell was discharged with a C/10 rate to a cell voltage of 2.2 V in order to ensure that all solid sulfur particles are dissolved as polysulfides in solution. This step is repeated after each

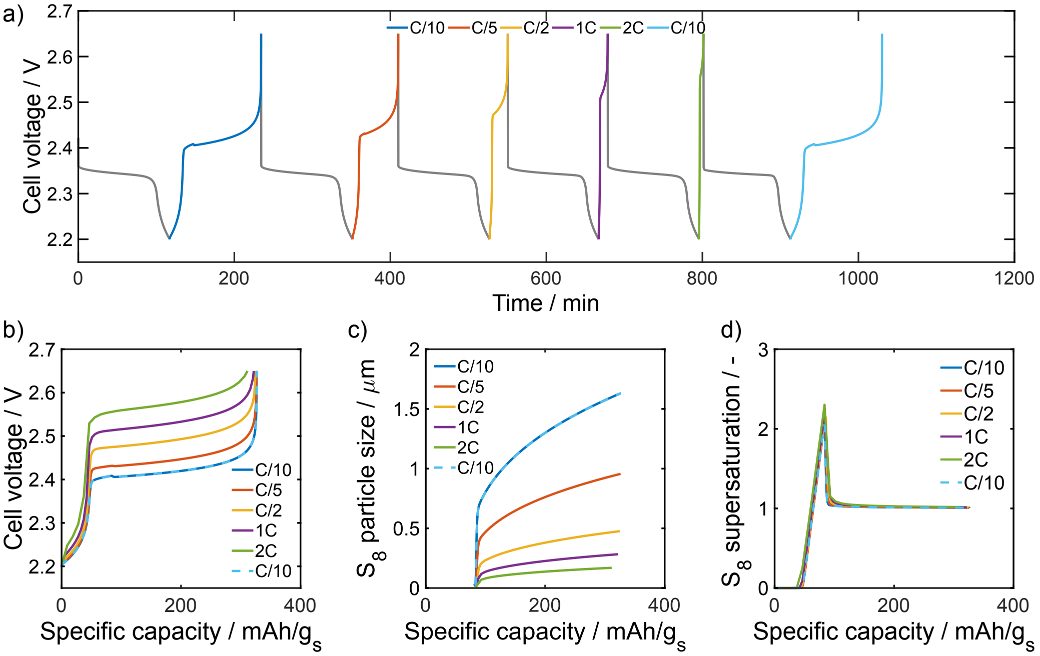

Figure 7: a) Simulated shallow cycling experiment investigating the effect of charge rate on b) the capacity and charge curve, c) S_8 particle size, and d) S_8 supersaturation.

charge cycle in order to ensure similar initial conditions for each current. The different charging currents corresponding to C-rates ranging from C/10 to 2C based on the theoretical sulfur capacity are highlighted by different colors in Figure 7 a). At the end of the protocol a C/10 charge process is simulated to demonstrate that the cycling does not affect the initial conditions. In Figure 7 b) the different charge curves are shown as function of specific capacity. At low currents the capacity of the charge process indicates a full oxidation of all polysulfide species in solution. The voltage curve shows a small feature in the plateau which is caused by the nucleation of S_8 particles. At higher current the overpotential increases and the small feature vanishes. Still, we see the formation of S_8 particles with smaller particle size in our simulations as shown in Figure 7 c). The particle size decreases with increasing currents which is in qualitative agreement with data published in the literature [30, 18]. Although smaller particles are potentially able to passivate the active electrode surface we see in our simulations only a small loss in capacity which is due to the choice of the cut-off voltage. At higher sulfur loading an additional loss in capacity due to surface passivation might be possible. The decrease in particle size with increasing currents is mainly due to the reduced time during which the particles are able to grow. In order to support this point Figure 7 d) shows the corresponding S_8 supersaturation, which is very similar for all currents and the maximum value at 2C is only marginally larger than the peak value at C/10. This demonstrates that the driving force for the nucleation of particles is similar in all cases and differences in the particle size can be mainly attributed to the difference in available time for nuclei formation and particle growth.

3.3. Interface design

The parameter studies above show that the morphology and precipitation kinetics can have a strong effect on the performance and capacity of the cell. One route to control the nucleation and growth process is by tuning the surface energy with suitable electrolyte additives. Another promising route is to modify the carbonaceous electrode surface in order to provide preferential adsorption sites. In the literature it was shown that e.g. nitrogen doping of the material improves the cycle life [7] and that materials with high affinity to sulfur like indium tin oxide or aluminum-doped zinc oxide are able to provide spatial control of the precipitation process [20, 17] which improves the capacity of the cell. However, in their study the authors [20] also show

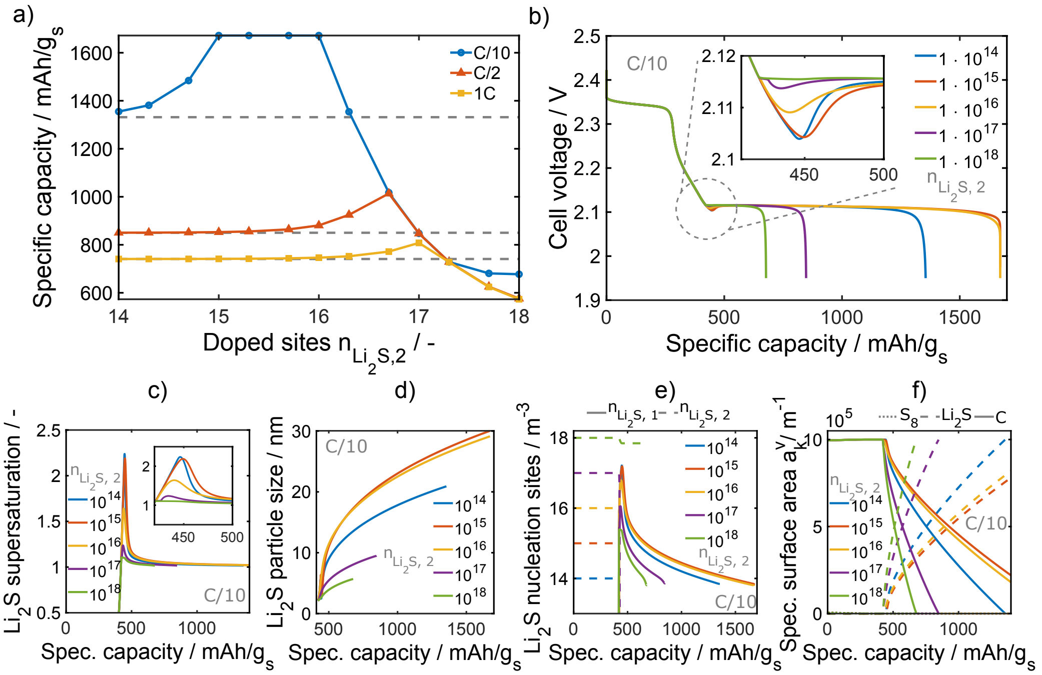

Figure 8: Effect of doped surface sites $n_{Li_2S,2}$ with high affinity towards Li_2S on a) the specific discharge capacity at various currents and b) the corresponding discharge curves at C/10 rate. The grey dashed line in a) indicates the undoped reference case. c) Li_2S supersaturation and d) particle size as function of initial doped nucleation sites. Figure 8 e) shows the available nucleation sites on the uncovered carbon surface $n_{Li_2S,1}$ and doped sites $n_{Li_2S,2}$, respectively. e) Evolution of specific surface area.

that electrodes consisting only of a material with high affinity have a very poor capacity. The model parameter controlling the affinity of Li_2S with the electrode material or more the specifically the nucleation site l is the contact angle θ_l. The overall number or surface density of nucleation sites is the second decisive parameter of the nucleation process. In our simulations we focus on the case of a surface which is doped with a material with a high affinity towards sulfur species resulting in a contact angle of Li_2S on the surface of only 30°. In order to assess the optimal degree of doping we vary the number of nucleation sites in our simulations such that nucleation events occur both on the carbon surface as well as on the doped sites. Results of this study are presented in Figure 8. Figure 8 a) shows the specific capacity of the doped materials for discharge currents corresponding to C/10, 1C and 2C as function of introduced doping sites $n_{Li_2S,2}$. At all currents doping of the materials has a beneficial effect on the capacity of the cell compared to the undoped case indicated by the grey dashed line. It is most pronounced at C/10 where small degrees of doping result in basically full conversion of the sulfur. However, at high doping levels the capacity drops rapidly to values far away from the theoretical capacity. Similar behavior can be observed at higher currents, however, the peak is shifted to higher doping contents and the sulfur is not fully utilized. This is in qualitative agreement with the studies on modified electrodes reported in the literature [20]. Figure 8 b) shows the corresponding discharge curves at C/10 rate for a subset of the doped materials. The discharge curves reflect the trend in discharge capacity discussed in Figure 8 a). As expected the initial discharge voltage during the dissolution of the sulfur particles is practically identical. The inset shows the interesting area of the Li_2S nucleation dip at around 450 mAh/g_S. The graph illustrates that a high doping level will reduce the voltage dip corresponding to the energy barrier which is needed for the nucleation of seed particles. At the highest doping level the voltage dip is almost negligible indicating immediate nucleation and growth as soon as the concentrations in the electrolyte are close to the solubility limit. Therefore, the same trend is reflected in the Li_2S supersaturation shown in Figure 8 c). The resulting evolution of Li_2S particle size is shown in Figure 8 d). At intermediate doping levels the particle size is the largest which has a beneficial effect on the capacity. Figure 8 f) shows the resulting evolution of specific surface area. The graph demonstrates that for larger particles the passivating effect of the Li_2S particles on the active carbon surface is less pronounced. In order to understand this trend it is helpful to have a look at the available nucleation sites in Figure 8 e). The solid line represents nucleation sites on the carbon surface calculated according to Eq. (35) and the dashed line shows available nucleation sites introduced by doping of the carbon. At the solubility limit of Li_2S at around 450 mAh/g_S the doped sites are consumed immediately serving as seed for the nucleation and growth process. Low numbers of nucleation seeds do not sufficiently reduce the supersaturation in the electrolyte (cf. Figure 8 c) in order to avoid substantial nucleation on the carbon surface. Resulting in a higher number of small particles blocking the surface. High doping levels on the other hand instantly provide a large number of preferential nucleation sites which even enhances the formation of small particles causing a rapid passivation of the surface. At intermediate doping levels the initial nucleation on preferred doping sites efficiently reduces the supersaturation and, thus, the nucleation on the carbon surface. This allows for the growth of preferential larger particles which maximizes the sulfur utilization. This study shows how the model presented in this work is able to contribute in finding improved materials for next-generation Li-S batteries.

4. Summary and conclusions

The formation and dissolution of solid phases during charge and discharge is an important factor for the energy and power density of future Li-S batteries. In the article we present a detailed model addressing the formation and dissolution of both Li_2S and S_8 during discharge and charge. Simulation results are in good qualitative agreement with in-*operando* data published in the literature [30]. Intensive parameter and sensitivity studies are performed in order access the most critical model parameters which need to be identified in dedicated experiments or ab-*initio* simulations. Especially, the model parameters determining the thermodynamics and kinetics of Li_2S precipitation were found to have a strong impact on the capacity of the cell during discharge. This indicates that an engineering of the electrode surface and modifications of the electrolyte system which affect the solubility and surface energy of Li_2S are an important component of a strategy to improve the performance of Li-S cells. Based on these results we focus on the influence of surface modifications and performed a design study investigating the effect of doping the carbon host structure. In agreement with data published in the literature the model predicts a beneficial effect of doped sites with a high affinity towards sulfur species. However, high doping levels reduce battery capacity suggesting that careful optimization of the doping level is needed which is certainly one possible application of our model. For Li-S cells with high energy density the sulfur loading has to be increased and at the same time high sulfur-to-electrolyte ratios are desirable. This development will amplify the effect of solid charge and discharge products and additional theoretical as well as experimental studies are required to investigate the effect of surface modifications under these conditions. For this purpose computationally more involved 2D and 3D continuum models of Li-S cells will need to be developed which are able to take into account the effect of the cell geometry and electrolyte distribution. The calculations will be able to reduce the development time of optimized electrode materials and will thus contribute to the improvement of Li-S technology.

Acknowledgments

The authors acknowledge support with computational resources provided by the state of Baden-Württemberg through bwHPC (bwForCluster JUSTUS) and the German Research Foundation (DFG) through grant no INST 40/467-1 FUGG.

[1] P. G. Bruce, S. A. Freunberger, L. J. Hardwick, J.-M. Tarascon, Li-O2 and Li-S batteries with high energy storage., Nat Mater 11 (1) (2012) 19–29. `doi:10.1038/nmat3191`.

[2] D. Bresser, S. Passerini, B. Scrosati, Recent progress and remaining challenges in sulfur-based lithium secondary batteries–a review., Chem Commun 49 (90) (2013) 10545–62. `doi:10.1039/c3cc46131a`.

[3] M. Barghamadi, A. Kapoor, C. Wen, A Review on Li-S Batteries as a High Efficiency Rechargeable Lithium Battery, J Electrochem Soc 160 (8) (2013) A1256–A1263. `doi:10.1149/2.096308jes`.

[4] S. Evers, L. F. Nazar, New approaches for high energy density lithium-sulfur battery cathodes, Accounts Chem Res 46 (5) (2013) 1135–1143. `doi:10.1021/ar3001348`.

[5] L. Chen, L. L. Shaw, Recent advances in lithium-sulfur batteries, J Power Sources 267 (2014) 770–783. `doi:10.1016/j.jpowsour.2014.05.111`.

[6] Y. Wang, E. Sahadeo, G. Rubloff, C.-f. Lin, High-capacity lithium sulfur battery and beyond : a review of metal anode protection layers and perspective of solid-state electrolytes, J Mater Sci 54 (5) (2019) 3671–3693. `doi:10.1007/s10853-018-3093-7`.

[7] L. Zhang, Y. Wang, Z. Niu, J. Chen, Advanced nanostructured carbon-based materials for rechargeable lithium-sulfur batteries, Carbon 141 (2019) 400–416. `doi:10.1016/j.carbon.2018.09.067`.

[8] S.-y. Li, W.-p. Wang, H. Duan, Y.-g. Guo, Recent progress on confinement of polysulfides through physical and chemical methods, J Energy Chem`doi:10.1016/j.jechem.2018.04.014`.

[9] D. Su, D. Zhou, C. Wang, G. Wang, Toward High Performance Lithium-Sulfur Batteries Based on Li_2S Cathodes and Beyond: Status, Challenges, and Perspectives, Adv Funct Mater 1800154 (2018) 1–23. `doi:10.1002/adfm.201800154`.

[10] H. Wang, W. Zhang, J. Xu, Z. Guo, Advances in Polar Materials for Lithium-Sulfur Batteries, Adv Funct Mater 1707520 (2018) 1–14. `doi:10.1002/adfm.201707520`.

[11] Y. Zhu, S. Wang, Z. Miao, Y. Liu, S.-l. Chou, Novel Non-Carbon Sulfur Hosts Based on Strong Chemisorption for Lithium-Sulfur Batteries, Small 14 (2018) 1801987. `doi:10.1002/smll.201801987`.

[12] M. Barghamadi, A. S. Best, A. I. Bhatt, A. F. Hollenkamp, M. Musameh, R. J. Rees, T. Rüther, Lithium-sulfur batteries - the solution is in the electrolyte, but is the electrolyte a solution?, Energy Environ Sci 7 (12) (2014) 3902–3920. `doi:10.1039/C4EE02192D`.

[13] S. S. Zhang, Liquid electrolyte lithium/sulfur battery: Fundamental chemistry, problems, and solutions, J Power Sources 231 (0) (2013) 153–162. `doi:10.1016/j.jpowsour.2012.12.102`.

[14] L. Wang, Y. Ye, N. Chen, Y. Huang, L. Li, F. Wu, R. Chen, Development and Challenges of Functional Electrolytes for High-Performance Lithium-Sulfur Batteries, Adv Funct Mater 1800919 (2018) 1–23. `doi:10.1002/adfm.201800919`.

[15] T. Cleaver, P. Kovacik, M. Marinescu, Commercializing Lithium Sulfur Batteries: Are We Doing the Right Research?, J Electrochem Soc 165 (1) (2018) A6029–A6033. `doi:10.1149/2.0071801jes`.

[16] C. Shen, J. Xie, M. Zhang, P. Andrei, M. Hendrickson, E. J. Plichta, J. P. Zheng, Understanding the role of lithium polysulfide solubility in limiting lithium-sulfur cell capacity, Electrochim Acta 248 (2017) 90–97. `doi:{10.1016/j.electacta.2017.07.123}`.

[17] H. Yao, G. Zheng, P.-C. Hsu, D. Kong, J. J. Cha, W. Li, Z. W. Seh, M. T. McDowell, K. Yan, Z. Liang, V. K. Narasimhan, Y. Cui, Improving lithium-sulphur batteries through spatial control of sulphur species deposition on a hybrid electrode surface, Nat Commun 5 (May) (2014) 1–9. `doi:10.1038/ncomms4943`.

[18] F. Y. Fan, W. C. Carter, Y.-M. Chiang, Mechanism and Kinetics of Li_2S Precipitation in Lithium-Sulfur Batteries, Adv Mater 27 (2015) 5203–5209. `doi:10.1002/adma.201501559`.

[19] L. C. H. Gerber, P. D. Frischmann, F. Y. Fan, S. E. Doris, X. Qu, A. M. Scheuermann, K. Persson, Y.-M. Chiang, B. A. Helms, Three-Dimensional Growth of Li_2S in Lithium-Sulfur Batteries Promoted by a Redox Mediator, Nano Lett 16 (1) (2016) 549–554. `doi:10.1021/acs.nanolett.5b04189`.

[20] F. Y. Fan, Y.-M. Chiang, Electrodeposition Kinetics in Li-S Batteries: Effects of Low Electrolyte/Sulfur Ratios and Deposition Surface Composition, J Electrochem Soc 164 (4) (2017) A917–A922. `doi:10.1149/2.0051706jes`.

[21] Y. Ren, T. Zhao, M. Liu, P. Tan, Y. Zeng, Modeling of lithium-sulfur batteries incorporating the effect of Li_2S precipitation, J Power Sources 336 (2016) 115–125. `doi:10.1016/j.jpowsour.2016.10.063`.

[22] N. A. Cañas, S. Wolf, N. Wagner, K. A. Friedrich, In-situ X-ray diffraction studies of lithium-sulfur batteries, J Power Sources 226 (2013) 313–319. `doi:10.1016/j.jpowsour.2012.10.092`.

[23] J. Nelson, S. Misra, Y. Yang, A. Jackson, Y. Liu, H. Wang, H. Dai, J. C. Andrews, Y. Cui, M. F. Toney, In Operando X-ray Diffraction and Transmission X-ray Microscopy of Lithium Sulfur Batteries, J Am Chem Soc 134 (14) (2012) 6337–6343. `doi:10.1021/ja2121926`.

[24] M. Cuisinier, P. E. Cabelguen, S. Evers, G. He, M. Kolbeck, A. Garsuch, T. Bolin, M. Balasubramanian, L. F. Nazar, Sulfur speciation in Li-S batteries determined by operando X-ray absorption spectroscopy, J Phys Chem Lett 4 (19) (2013) 3227–3232. `doi:10.1021/jz401763d`.

[25] Y. Gorlin, A. Siebel, M. Piana, T. Huthwelker, H. Jha, G. Monsch, F. Kraus, H. A. Gasteiger, M. Tromp, Operando Characterization of Intermediates Produced in a Lithium-Sulfur Battery, J Electrochem Soc 162 (7) (2015) A1146–A1155. `doi:10.1149/2.0081507jes`.

[26] T. A. Pascal, C. D. Pemmaraju, D. Prendergast, X-ray spectroscopy as a probe for lithium polysulfide radicals, Phys Chem Chem Phys 17 (2015) 7743–7753. `doi:10.1039/C4CP05316H`.

[27] M. Vijayakumar, N. Govind, E. Walter, S. D. Burton, A. Shukla, A. Devaraj, J. Xiao, J. Liu, C. Wang, A. Karim, S. Thevuthasan, Molecular structure and stability of dissolved lithium polysulfide species., Phys Chem Chem Phys 16 (22) (2014) 10923–32. `doi:10.1039/c4cp00889h`.

[28] J. Conder, R. Bouchet, S. Trabesinger, C. Marino, L. Gubler, C. Villevieille, Direct observation of lithium polysulfides in lithium-sulfur batteries using operando X-ray diffraction, Nat Energy 2 (6). `doi:10.1038/nenergy.2017.69`.

[29] C.-n. Lin, W.-c. Chen, Y.-f. Song, C.-c. Wang, L.-d. Tsai, N.-l. Wu, Understanding dynamics of polysulfide dissolution and re-deposition in working lithium-sulfur battery by in-operando transmission X-ray

microscopy, J Power Sources 263 (2014) 98–103. `doi:10.1016/j.jpowsour.2014.04.003`.

[30] S.-H. Yu, X. Huang, K. Schwarz, R. Huang, T. A. Arias, J. D. Brock, H. D. Abruña, Direct visualization of sulfur cathodes: new insights into Li-S batteries via operando X-ray based methods, Energy Environ Sci 11 (1) (2018) 202–210. `doi:10.1039/C7EE02874A`.

[31] K. Kumaresan, Y. Mikhaylik, R. E. White, A Mathematical Model for a Lithium-Sulfur Cell, J Electrochem Soc 155 (8) (2008) A576. `doi:10.1149/1.2937304`.

[32] J. P. Neidhardt, D. N. Fronczek, T. Jahnke, T. Danner, B. Horstmann, W. G. Bessler, A Flexible Framework for Modeling Multiple Solid, Liquid and Gaseous Phases in Batteries and Fuel Cells, J Electrochem Soc 159 (9) (2012) A1528–A1542. `doi:10.1149/2.023209jes`.

[33] M. Ghaznavi, P. Chen, Sensitivity analysis of a mathematical model of lithium-sulfur cells: Part I: Applied discharge current and cathode conductivity, J Power Sources 257 (2014) 394–401. `doi:10.1016/j.jpowsour.2013.10.135`.

[34] M. Ghaznavi, P. Chen, Sensitivity analysis of a mathematical model of lithium-sulfur cells: Part II: Precipitation reaction kinetics and sulfur content, J Power Sources 257 (2014) 402–411. `doi:10.1016/j.jpowsour.2013.12.145`.

[35] M. Ghaznavi, P. Chen, Analysis of a Mathematical Model of Lithium-Sulfur Cells Part III: Electrochemical Reaction Kinetics, Transport

Properties and Charging, Electrochim Acta 137 (2014) 575–585. `doi:10.1016/j.electacta.2014.06.033`.

[36] M. Marinescu, T. Zhang, G. J. Offer, A zero dimensional model of lithium-sulfur batteries during charge and discharge., Phys Chem Chem Phys 18 (1) (2016) 584–93. `doi:10.1039/c5cp05755h`.

[37] T. Zhang, M. Marinescu, L. O'Neill, M. Wild, G. Offer, Modeling the voltage loss mechanisms in lithium-sulfur cells: the importance of electrolyte resistance and precipitation kinetics, Phys Chem Chem Phys 17 (35) (2015) 22581–6. `doi:10.1039/c5cp03566j`.

[38] D. N. Fronczek, W. G. Bessler, Insight into lithium-sulfur batteries: Elementary kinetic modeling and impedance simulation, J Power Sources 244 (2013) 183–188. `doi:10.1016/j.jpowsour.2013.02.018`.

[39] Y. V. Mikhaylik, J. R. Akridge, Polysulfide Shuttle Study in the Li/S Battery System, J Electrochem Soc 151 (11) (2004) A1969. `doi:10.1149/1.1806394`.

[40] A. F. Hofmann, D. N. Fronczek, W. G. Bessler, Mechanistic modeling of polysulfide shuttle and capacity loss in lithium-sulfur batteries, J Power Sources 259 (2014) 300–310. `doi:10.1016/j.jpowsour.2014.02.082`.

[41] T. Danner, G. Zhu, A. F. Hofmann, A. Latz, Modeling of nanostructured cathodes for improved lithium-sulfur batteries, Electrochim. Acta 184 (2015) 124–133. `doi:10.1016/j.electacta.2015.09.143`.

[42] V. Thangavel, K.-H. Xue, Y. Mammeri, M. Quiroga, A. Mastouri,

C. Guéry, P. Johansson, M. Morcrette, A. A. Franco, A Microstructurally Resolved Model for Li-S Batteries Assessing the Impact of the Cathode Design on the Discharge Performance, J Electrochem Soc 163 (13) (2016) A2817–A2829. `doi:10.1149/2.0051614jes`.

[43] C. Xiong, T. Zhao, Y. Ren, H. Jiang, X. Zhou, Mathematical modeling of the charging process of Li-S batteries by incorporating the size-dependent Li2S dissolution, Electrochim Acta 296 (2019) 954–963. `doi:10.1016/j.electacta.2018.11.159`.

[44] P. Andrei, C. Shen, J. P. Zheng, Theoretical and experimental analysis of precipitation and solubility effects in lithium-sulfur batteries, Electrochim Acta 284 (2018) 469–484. `doi:{10.1016/j.electacta.2018.07.045}`.

[45] P. P. R. M. L. Harks, C. B. Robledo, T. W. Verhallen, P. H. L. Notten, F. M. Mulder, The Significance of Elemental Sulfur Dissolution in Liquid Electrolyte Lithium Sulfur Batteries, Adv Energy Mater 7 (3) (2017) 1601635. `doi:10.1002/aenm.201601635`.

[46] Z. Liu, P. P. Mukherjee, Mesoscale Elucidation of Surface Passivation in the Li-Sulfur Battery Cathode, ACS Appl. Mater. Interfaces 9 (6) (2017) 5263–5271. `doi:10.1021/acsami.6b15066`.

[47] A. Mistry, P. P. Mukherjee, Precipitation?Microstructure Interactions in the Li-Sulfur Battery Electrode, J. Phys. Chem. C 121 (47) (2017) 26256–26264. `doi:10.1021/acs.jpcc.7b09997`.

[48] N. T. K. Thanh, N. Maclean, S. Mahiddine, Mechanisms of nucleation and growth of nanoparticles in solution, Chem Rev 114 (15) (2014) 7610–7630. `doi:10.1021/cr400544s`.

[49] B. Horstmann, T. Danner, W. G. Bessler, Precipitation in aqueous lithium-oxygen batteries: a model-based analysis, Energy Environ Sci 6 (4) (2013) 1299–1314. `doi:10.1039/c3ee24299d`.

[50] H. Park, H. S. Koh, D. J. Siegel, First-Principles Study of Redox End Members in Lithium-Sulfur Batteries, J Phys Chem C 119 (9) (2015) 4675–4683. `doi:10.1021/jp513023v`.

[51] F. Y. Fan, M. S. Pan, K. C. Lau, R. S. Assary, W. H. Woodford, L. A. Curtiss, W. C. Carter, Y.-M. Chiang, Solvent Effects on Polysulfide Redox Kinetics and Ionic Conductivity in Lithium-Sulfur Batteries, J Electrochem Soc 163 (14) (2016) A3111–A3116. `doi:10.1149/2.1181614jes`.

[52] Y.-C. Lu, Q. He, H. A. Gasteiger, Probing the Lithium-Sulfur Redox Reactions: A Rotating-Ring Disk Electrode Study, J Phys Chem C 118 (11) (2014) 5733–5741. `doi:10.1021/jp500382s`.

[53] A. J. Conder, C. Villevieille, L. Gubler, R. Bouchet, L. Gubler, R. Bouchet, Electrochemical impedance spectroscopy of a Li?S battery: Part 1. Influence of the electrode and electrolyte compositions on the impedance of symmetric cells, Electrochim Acta 244. `doi:10.1016/j.electacta.2017.05.041`.

[54] J. Conder, C. Villevieille, S. Trabesinger, P. Novák, L. Gubler, R. Bouchet, Electrochimica Acta Electrochemical impedance spectroscopy of a Li-S battery: Part 2. Influence of separator chemistry on the lithium electrode / electrolyte interface, Electrochim Acta 255 (2017) 379–390. `doi:10.1016/j.electacta.2017.09.148`.

[55] Q. He, Y. Gorlin, Y.-c. Lu, M. U. M. Patel, H. A. Gasteiger, Unraveling the Correlation between Solvent Properties and Sulfur Redox Behavior in Lithium-Sulfur Batteries, J Electrochem Soc 165 (16) (2018) 2–8. `doi:10.1149/2.0991816jes`.

[56] A. Berger, A. T. S. Freiberg, A. Siebel, R. Thomas, M. U. M. Patel, M. Tromp, H. A. Gasteiger, Y. Gorlin, The Importance of Chemical Reactions in the Charging Process of Lithium-Sulfur Batteries, J Electrochem Soc 165 (7) (2018) 1288–1296. `doi:10.1149/2.0181807jes`.

[57] F. Hintz, U. Krewer, P. Sch, Electrochemical analysis of the reaction mechanism of sulfur reduction as a function of state of charge, Electrochim Acta 295 (2019) 926–933. `doi:10.1016/j.electacta.2018.08.153`.

[58] C. Barchasz, F. Molton, C. Duboc, Lithium/Sulfur Cell Discharge Mechanism: An Original Approach for Intermediate Species Identification, Anal Chem 84 (2012) 3973–3980. `doi:10.1021/ac2032244`.

[59] N. A. Cañas, D. N. Fronczek, N. Wagner, A. Latz, K. A. Friedrich, Experimental and Theoretical Analysis of Products and Reaction Inter-

mediates of Lithium-Sulfur Batteries, J Phys Chem C 118 (23) (2014) 12106–12114. `doi:10.1021/jp5013208`.

[60] X. Chen, T. Hou, K. A. Persson, Q. Zhang, Combining theory and experiment in lithium-sulfur batteries: Current progress and future perspectives, Mater Today 22 (February) (2019) 142–158. `doi:10.1016/j.mattod.2018.04.007`.

[61] M. Z. Bazant, Theory of Chemical Kinetics and Charge Transfer based on Nonequilibrium Thermodynamics, Accounts Chem Res 46 (5). `doi:10.1021/ar300145c`.

[62] A. Latz, J. Zausch, Thermodynamic derivation of a Butler?Volmer model for intercalation in Li-ion batteries, Electrochim. Acta 110 (2013) 358–362. `doi:10.1016/j.electacta.2013.06.043`.
URL `http://dx.doi.org/10.1016/j.electacta.2013.06.043http://linkinghub.elsevier.com/retrieve/pii/S0013468613011493https://linkinghub.elsevier.com/retrieve/pii/S0013468613011493`

[63] H. Vehkamäki, A. Määttänen, A. Lauri, I. Napari, M. Kulmala, Technical Note: The heterogeneous Zeldovich factor, Atmos Chem Phys 7 (2) (2007) 309–313. `doi:10.5194/acp-7-309-2007`.

[64] S. Jeschke, P. Johansson, Predicting the Solubility of Sulfur: A COSMO-RS-Based Approach to Investigate Electrolytes for Li-S Batteries, Chem - A Eur J 23 (38) (2017) 9130–9136. `doi:10.1002/chem.201701011`.

[65] C. Park, M. Kanduč, R. Chudoba, A. Ronneburg, S. Risse, M. Ballauff, J. Dzubiella, Molecular simulations of electrolyte structure and dynamics in lithium-sulfur battery solvents, J Power Sources 373 (July 2017) (2018) 70–78. `doi:10.1016/j.jpowsour.2017.10.081`.

[66] M. Safari, C. Y. Kwok, L. F. Nazar, Transport Properties of Polysulfide Species in Lithium-Sulfur Battery Electrolytes: Coupling of Experiment and Theory, ACS Cent Sci 2 (8) (2016) 560–568. `doi:10.1021/acscentsci.6b00169`.

[67] A. F. Holleman, E. Wiberg, Lehrbuch der anorganischen Chemie, 33rd Edition, Walter de Gruyter, Berlin, New York, 1995.

[68] D. R. Lide, CRC handbook of chemistry and physics, 87th Edition, CRC press, 2006.

List of Tables

Parameter	**Value**	**Meaning**	**Source**
Transport parameters			
Electrolyte			
η_{elyte}	0.01 Pa s	Electrolyte viscosity (48) ($c_S = 0.1$ mol/l)	[51]
$D_{\mathrm{Li^+}}$	$4.7 \cdot 10^{-10}\ \frac{\mathrm{m^2}}{\mathrm{s}}$	$\mathrm{Li^+}$ diffusion coefficient	[65]
$D_{\mathrm{TFSI^-}}$	$3.8 \cdot 10^{-10}\ \frac{\mathrm{m^2}}{\mathrm{s}}$	$\mathrm{TFSI^-}$ diffusion coefficient	[65]
$D_{\mathrm{NO_3^-}}$	$3.9 \cdot 10^{-10}\ \frac{\mathrm{m^2}}{\mathrm{s}}$	$\mathrm{NO_3^-}$ diffusion coefficient	[65]
$D_{\mathrm{S_8}}$	$10 \cdot 10^{-10}\ \frac{\mathrm{m^2}}{\mathrm{s}}$	$\mathrm{S_8}$ diffusion coefficient	[45]
$D_{\mathrm{S_6^{2-}}}$	$5.3 \cdot 10^{-10}\ \frac{\mathrm{m^2}}{\mathrm{s}}$	$\mathrm{S_6^{2-}}$ diffusion coefficient	[66]
$D_{\mathrm{S_4^{2-}}}$	$7.6 \cdot 10^{-10}\ \frac{\mathrm{m^2}}{\mathrm{s}}$	$\mathrm{S_4^{2-}}$ diffusion coefficient	[66]
$D_{\mathrm{S^{2-}}}$	$0.61 \cdot 10^{-10}\ \frac{\mathrm{m^2}}{\mathrm{s}}$	$\mathrm{S^{2-}}$ diffusion coefficient	*
Carbon			
κ_{elode}	$1\ \frac{\mathrm{S}}{\mathrm{m}}$	Electronic conductivity	*
c_{elode}	$0.1\ \frac{\mathrm{F}}{\mathrm{m^2}}$	Double layer capacity	*
Electrochemical parameters			
$3/8\ \mathbf{S}_8^{(l)} + \mathbf{e}^- \rightleftharpoons 4/8\ \mathbf{S}_6^{2-}$			
$k^{f,0}$	$6.189 \cdot 10^{-9}\ \frac{\mathrm{mol}}{\mathrm{m}^2 s}$	Frequency factor of reaction	**
α	0.5	Symmetry factor of transition state	**
$U_{\mathrm{eq}}^{\ominus}$	2.45 V	OCP at reference conditions	**
$1\ \mathbf{S}_6^{2-} + \mathbf{e}^- \rightleftharpoons 3/2\ \mathbf{S}_4^{2-}$			
$k^{f,0}$	$1.526 \cdot 10^{-8}\ \frac{\mathrm{mol}}{\mathrm{m}^2 s}$	Frequency factor of reaction	**
α	0.5	Symmetry factor of transition state	**

Continued on next page

Continued from previous page

Parameter	**Value**	**Meaning**	**Source**
$U_{\mathrm{eq}}^{\ominus}$	2.25 V	OCP at reference conditions	**
$1/6\ \mathbf{S_4^{2-}} + \mathbf{e^-} \rightleftharpoons 4/6\ \mathbf{S^{2-}}$			
$k^{f,0}$	$5.153 \cdot 10^{-7}\ \frac{\mathrm{mol}}{\mathrm{m}^2 s}$	Frequency factor of reaction	**
α	0.5	Symmetry factor of transition state	**
$U_{\mathrm{eq}}^{\ominus}$	2.14 V	OCP at reference conditions	**
$\mathbf{Li^+} + \mathbf{e^-} \rightleftharpoons \mathbf{Li}^{(s)}$			
$k^{f,0}$	$4.084 \cdot 10^{-6}\ \frac{\mathrm{mol}}{\mathrm{m}^2 s}$	Frequency factor of reaction	[33]
α	0.5	Symmetry factor of transition state	**
$U_{\mathrm{eq}}^{\ominus}$	0.0 V	Li reference electrode	
		Solid phase dissolution & growth	
$\mathbf{S_8^{(s)}}$			
$\rho_{\mathrm{S_8^{(s)}}}$	$2070.4\ \frac{\mathrm{kg}}{\mathrm{m}^3}$	Density	[67]
$MW_{\mathrm{S_8^{(s)}}}$	$0.2565\ \frac{\mathrm{kg}}{\mathrm{mol}}$	Molecular weight	[68]
$K^{\mathrm{sp}}_{\mathrm{S_8^{(s)}}}$	$3.99\ \frac{\mathrm{mol}}{\mathrm{m}^3}$	Solubility	[64]
$\gamma_{\mathrm{S_8^{(s)}}}$	$7.8762 \cdot 10^{-4}\ \frac{\mathrm{J}}{\mathrm{m}^2}$	Surface energy	[50]
$k^0_{\mathrm{S_8^{(s)}}}$	$9.0 \cdot 10^{-6}\ \frac{\mathrm{m}}{\mathrm{s}}$	Growth factor	**
$\mathbf{Li_2S}$			
$\rho_{\mathrm{Li_2S}}$	$1659.9\ \frac{\mathrm{kg}}{\mathrm{m}^3}$	Density	[68]
$MW_{\mathrm{Li_2S}}$	$0.0459\ \frac{\mathrm{kg}}{\mathrm{mol}}$	Molecular weight	[68]
$K^{\mathrm{sp}}_{\mathrm{Li_2S}}$	$1.55 \cdot 10^{7}\ \frac{\mathrm{mol}^3}{\mathrm{m}^9}$	Solubility	*
$\gamma_{\mathrm{Li_2S}}$	$7.7 \cdot 10^{-3}\ \frac{\mathrm{J}}{\mathrm{m}^2}$	Surface energy	* based on [50]

Continued on next page

Continued from previous page

Parameter	**Value**	**Meaning**	**Source**
$k^0_{\mathrm{Li_2S}}$	$1.0 \cdot 10^{-7}\ \frac{\mathrm{m}}{\mathrm{s}}$	Growth factor	*

* assumed parameter, **fit to experimental data

Table 2: Transport, kinetic, and thermodynamic parameters of species and phases considered in this work.

Cathode	**Thickness**	100 µm
	Volume elements	1
	Surface area	$1.0{\cdot}10^6$ m^{-1}
	Bruggeman coefficient	1.5
	Phases	
	Carbon & Binder	0.19
	$S_8^{(s)}$	0.012
	Size range	$1{\cdot}10^{-9}$ - $1{\cdot}10^{-5}$ m
	Volume elements	10 per decade
	Contact angle	30°
	Li_2S	0.0
	Size range	$1{\cdot}10^{-9}$ - $1{\cdot}10^{-5}$ m
	Volume elements	20 per decade
	Contact angle	120°
	Electrolyte	0.798
	(Li^+, $TFSI^-$, NO_3^-, $S_8^{(l)}$, S_6^{2-}, S_4^{2-}, S^{2-})	(1200.058, 1000, 200,3.99, $1{\cdot}10^{-3}$, 0.02787, $1{\cdot}10^{-6}$ mol/m^3)
Separator	**Thickness**	100 µm
	Volume elements	5
	Bruggeman coefficient	1.0
	Phases	
	Solid	0.2
	Electrolyte	0.8
	(Li^+, $TFSI^-$, NO_3^-, $S_8^{(l)}$, S_6^{2-}, S_4^{2-}, S^{2-})	(1200.058, 1000, 200, 3.99, $1{\cdot}10^{-3}$, 0.02787, $1{\cdot}10^{-6}$ mol/m^3)

Table 1: Structural parameters of the standard geometry studied in this work. In the case of concentrations, volume fractions, and surface areas initial values are given which are subject to changes during the simulations.

List of Figures